2011

Assessment of the Dependence of Ventilation Image Calculation from 4D-CT on Deformation and Ventilation Algorithms

Kujtim Latifi
University of South Florida, kujtim@gmail.com

Assessment of the Dependence of Ventilation Image Calculation from 4D-CT on Deformation and Ventilation Algorithms

by

Kujtim Latifi

A dissertation submitted in partial fulfillment
of the requirements for the degree of
Doctor of Philosophy
Department of Physics
College of Arts and Sciences
University of South Florida

Co-Major Professor: Kenneth Forster, Ph.D.
Co-Major Professor: Sagar Pandit, Ph. D.
Geoffrey Zhang, Ph.D.
Vladimir Feygelman, Ph.D.
Lilia Woods, Ph.D.
Dale Johnson, Ph.D.

Date of Approval:
November 7, 2011

Keywords: Lung Function, Deformable Image Registration, Ventilation Imaging, Radiotherapy, Lung Cancer

DEDICATION

To my family.

ACKNOWLEDGMENTS

I would like to acknowledge my two advisors at Moffitt Cancer Center, Drs. Kenneth Forster and Geoffrey Zhang, without their help and support this work could not have been accomplished. With special thanks to the entire Radiation Oncology staff at Moffitt whose support has been invaluable, specifically to Dr. Vladimir Feygelman for his advice, and for being a member of my doctoral committee. I am also grateful to my friends at Moffitt, Dan and Jake, for helping me keep my sanity during this time.

I would like to express my sincere gratitude to the Department of Physics at the University of South Florida, especially to Drs. Dale Johnson, Sagar Pandit, and Lilia Woods for being members of my doctoral committee, for their input, and accessibility. In particular, my appreciation is extended to Dr. Dale Johnson for his notable support and patience.

Finally, and most importantly, I would like to thank my wife Erjeta. Her patience, support, encouragement, and unwavering love were undeniably the foundation upon which the past few years of my life have been built upon. My parents, Xhelal and Mirvete, receive my deepest gratitude for their faith in me and for allowing me to be as ambitious as I have ever wanted to be. It was under their watchful eye that I gained so much drive along with the ability to tackle challenges head on. Last but not least, I would

like to thank Erjeta's parents, Ymer and Afërdita Toska, who provided me unending encouragement and support throughout the completion of my graduate studies.

TABLE OF CONTENTS

LIST OF TABLES

LIST OF FIGURES

ABSTRACT

Ventilation imaging using 4D-CT is a convenient and cost effective functional imaging methodology which might be of value in radiotherapy treatment planning to spare functional lung volumes. To calculate ventilation imaging from 4D-CT we must use deformable image registration (DIR). This study validates the DIR methods and investigates the dependence of calculated ventilation on DIR methods and ventilation algorithms.

The first hypothesis is if ventilation algorithms are robust then they will be insensitive to the precise DIR used provided the DIR is accurate. The second hypothesis is that the change in Houndsfield Unit (HU) method is less dependent on the DIR used and depends more on the CT image quality due to the inherent noise of HUs in normal CT imaging.

DIR of the normal end expiration and inspiration phases of the 4D-CT images was used to correlate the voxels between the two respiratory phases. All DIR algorithms were validated using a 4D pixel-based and point-validated breathing thorax model, consisting of a 4D-CT image data set along with associated landmarks. Three different DIR algorithms, Optical Flow (OF), Diffeomorphic Demons (DD) and Diffeomorphic Morphons (DM), were retrospectively applied to the same group of 10 esophagus and 10

lung cancer cases all of which had associated 4D-CT image sets that encompassed the entire lung volume. Three different ventilation calculation algorithms were compared (Jacobian, ΔV, and HU) using the Dice similarity coefficient comparison.

In the validation of the DIR algorithms, the average target registration errors with one standard deviation for the DIR algorithms were 1.6 ± 0.7 mm, maximum 3.1 mm for OF, 1.3 ± 0.6 mm, maximum 3.3 mm for DM, 1.3 ± 0.6 mm, maximum 2.8 mm for DD, indicating registration errors were within 2 voxels.

Dependence of ventilation images on the DIR was greater for the ΔV and the Jacobian methods than for the HU method. The Dice similarity coefficient for 20% of low ventilation volume for ΔV was 0.33 ± 0.03 between OF and DM, 0.44 ± 0.05 between OF and DD and 0.51 ± 0.04 between DM and DD. The similarity comparisons for Jacobian was 0.32 ± 0.03, 0.44 ± 0.05 and 0.51 ± 0.04 respectively, and for HU 0.53 ± 0.03, 0.56 ± 0.03 and 0.76 ± 0.04 respectively.

Dependence of ventilation images on the ventilation method used showed good agreement between the ΔV and Jacobian methods but differences between these two and the HU method were significantly greater. Dice similarity coefficient for using OF as DIR was 0.86 ± 0.01 between ΔV and Jacobian, 0.28 ± 0.04 between ΔV and HU and 0.28 ± 0.04 between Jacobian and HU respectively. When using DM or DD as DIR, similar values were obtained when comparing the different ventilation calculation

methods. The similarity values for 20% of the high ventilation volume were close to those found for the 20% low ventilation volume.

Mean target registration error for all three DIR methods was within one voxel suggesting that the registration done by either of the methods is quite accurate. Ventilation calculation from 4D-CT demonstrates some degree of dependency on the DIR algorithm employed. Similarities between ΔV and Jacobian are higher than between ΔV and HU and Jacobian and HU. This shows that ΔV and Jacobian are very similar, but HU is a very different ventilation calculation method.

CHAPTER 1 INTRODUCTION

According to the American Cancer Society, cancer is the second-leading cause of death in the United States after heart disease. [1] Twenty-nine percent of these cancer caused deaths were lung cancer patients, making lung cancer the biggest single cancer killer of both men and women. [1] Lung cancer is generally diagnosed in the later stages when the disease has created a large tumor burden, thus diminishing the possibility for cure. Treatment options typically include surgery, chemotherapy, and radiotherapy, whether used singly or in combination. Radiotherapy is utilized in up to half of lung cancer patients at some point after their cancer diagnosis.

It is well known that lung function is not uniform and there is a wide range of ventilation and perfusion levels throughout the lung. Previous studies evaluating the risks of pulmonary toxicity reported that the two best predictors were the volume of lung receiving 20 Gy [2, 3] and alternatively the mean radiation dose to normal lung. [4] To irradiate lung tumors, normal lung will also be irradiated, in addition the formation of clinical target volume (CTV[1]), internal target volume (ITV[2]), and planning target volume

[1] The CTV consists of the tumor volume and any other tissue with presumed tumor.
[2] The ITV is the volume that includes the CTV with an internal margin added to account for motion of the CTV.

(PTV[3]) expansions all include normal lung. This requirement to irradiate normal lung creates a necessary compromise between killing tumor cells while simultaneously limiting the dose to healthy tissues to minimize pulmonary toxicity. Many lung patients have compromised health before treatment for lung cancer, and chronic obstructive pulmonary disease (COPD) is common in these patients. Because they typically have diminished pulmonary reserve, radiation toxicities such as pneumonitis or fibrosis can be highly toxic and in some cases even fatal. Radiation pneumonitis usually develops in the first few weeks to months after beginning radiation therapy treatments. The symptoms of pneumonitis are shortness of breath, cough, and fever. Pulmonary fibrosis is the scarring of lung tissue and develops much later after radiation therapy, over moths to years, and leads to permanent impairment of oxygen transfer. Analogously to the lung, radiation dose constraints are placed on other critical structures such as the spinal cord, heart, and esophagus.

To help predict radiation toxicity, many researchers have tried to model the effects of radiation by examining how much normal tissue receives a given dose. [5] There has been much work presented on normal tissue complication probability (NTCP) models for the lung.[6-10] NPTCP is based on the assumption that the probability of complications follows a sigmoidal dose-response relationship. NTCP relies on mathematical models based on the tolerance of radiation dose to the whole organ and the steepness of the dose-response curve to calculate the probability of damage to the lung due to radiation. [11, 12] Emami et al [5] compiled data on tolerance dose values for uniform radiation of 28 critical

[3] The PTV is the volume that includes the ITV as well as a set-up margin to account for patient movement and set-up uncertainties.

structures. In another article Burman et al [13] fit the tolerance dose data to a NTCP model by Lyman. [12] The Lyman model is defined for uniform irradiation of organs. However, normal organs are usually not irradiated uniformly and as a result dose volume histogram (DVH) reduction algorithms were designed to convert a non uniform dose distribution to a uniform distribution. [14, 15] A DVH reduction algorithm based on the Lyman model was introduced by Kutcher and Burman [11], often referred to as the Lyman-Kutcher-Burman (LKB) model. This model is used as an auxiliary tool to evaluate and compare radiation treatment plans.

All the current models for radiation toxicity of the lung, cited above, are based on a uniformly functioning lung. Although most people have redundant pulmonary reserve, it is well known that lung function is not uniform and there is a wide range of ventilation and perfusion levels throughout the lung. [16-18] In particular, lung cancer patients have been shown to have regions of lung with poor ventilation. Jeraj et al suggest that imaging of normal tissue function may be useful in reducing normal tissue toxicity. [19]

1.1 Ventilation

The major function of the lung is to exchange carbon dioxide for oxygen in the blood. As the diaphragm depresses and the chest expands, the lung volume increases and a pressure gradient is created forcing air to flow into lungs. CO_2 is exchanged for O_2 in pulmonary capillaries. Oxygen (O_2), which is delivered to alveoli by ventilation, diffuses into pulmonary capillary blood and is carried away by the blood flow. Carbon dioxide

(CO_2), which is delivered to the alveoli in the venous blood, diffuses into the alveoli through the pulmonary capillaries and is removed from the alveoli by ventilation. As the diaphragm moves back up and the chest wall compresses the lung, the lung volume decreases forcing the CO_2 rich air out of the lungs.

Good air and blood flow are required for adequate oxygen – carbon dioxide exchange. Regional ventilation can be reduced in lung cancer patients for various reasons, and patients with COPD are thought to have significant regions of poor ventilation. Larger lung tumors can also obstruct the bronchus or bronchioles, causing the collapse of lung volume distal to the obstruction. If a radiation oncologist or even a surgeon knew which parts of the lung functioned properly and which did not, they could potentially spare highly functional lung while still treating the cancer.

A number of different imaging modalities can be employed to image and analyze lung function, including nuclear scintigraphy, [20] single photon emission computed tomography (SPECT), [18, 21-24] positron emission tomography (PET), [25, 26] magnetic resonance imaging (MRI),[27, 28] and CT. [29-38] These methods are described below.

1.1.1 Ventilation Imaging with SPECT

The current gold standard for imaging ventilation involves the acquisition of single photon emission computed tomography (SPECT) image. The image is acquired

after the patient breathes ^{99m}Tc-diethylene-triamine pentaacetate (DTPA) radioaerosol or ^{133}Xe radioactive gas. For ventilation studies using the radioaerosol technique, patients breathe the DTPA for a few minutes then equilibrium and washout scans are taken continuously. The average size of aerosol particles is close to 1.0 μm making them susceptible to deposition in central airwaves. [18, 39] Therefore, the aerosol technique is only good at detecting regions with low gamma ray emissions and thus low regional ventilation. [18, 23, 40-42] Figure 1 is an illustration of ventilation/perfusion using SPECT-CT. Coloring is according to a relative scale with low ventilation regions in darker color.

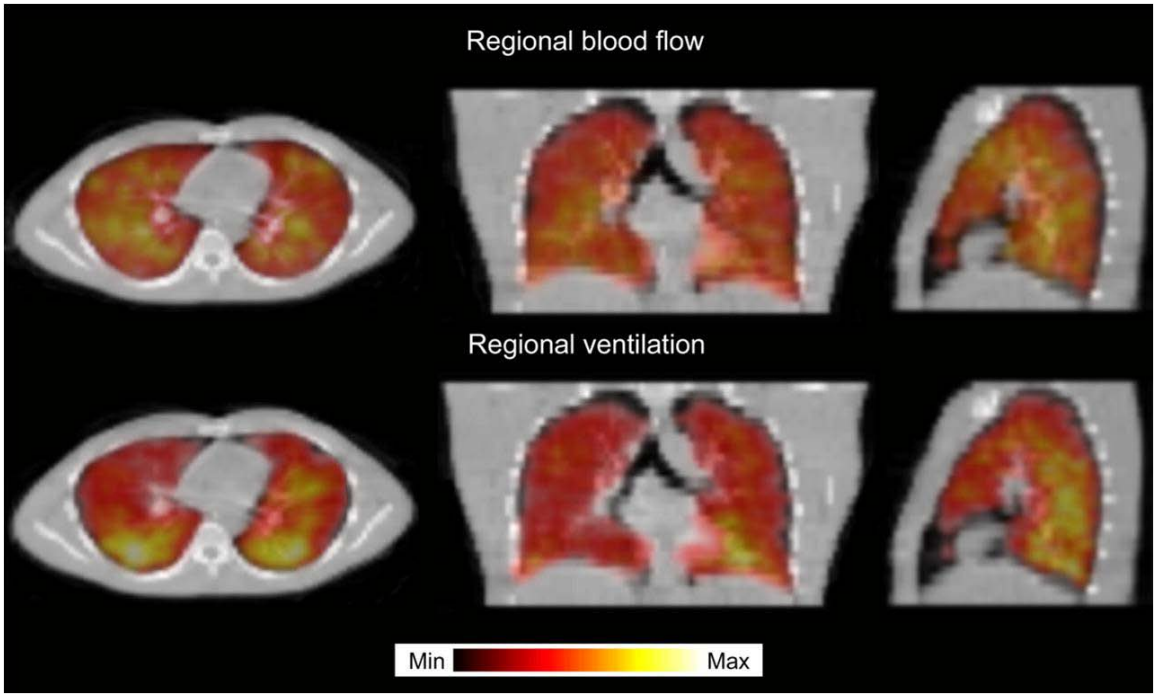

Figure 1. Ventilation/perfusion image with SPECT-CT. Coloring is according to a relative scale for each image. CT images are in grey, ventilation/perfusion images are colored. Used with permission. [18]

Dynamic ^{133}Xe ventilation imaging is a useful tool for accurately assessing ventilation defects. An image is usually taken during or right after inhalation of ^{133}Xe radioactive gas. Then washout images are taken while the patient breathes room air. Regions of radioactive gas retention are indicative of ventilation defects. [24] Additionally, with a dynamic SPECT study a matrix of half clearance time can be calculated and yields relative ventilation maps. Ventilation imaging with ^{133}Xe is useful for studying abnormalities in regional ventilation in patients with obstructive pulmonary disease. However, the low energy of ^{133}Xe (80 keV) results in low spatial resolution compared to ^{99m}Tc.

Other radionuclides used for imaging lung function with SPECT are ^{99m}Tc Technegas and ^{99m}Kr. Although those two methods have been shown to be very accurate in imaging ventilation, they are not commonly used in the clinic. [18, 24] Technegas is not approved by the Food and Drug Administration for use in the United States, and due to its very short half-life (13 s) the use of ^{99m}Kr in the clinic is quite difficult if not impossible. A limitation of the SPECT method compared to other imaging modalities is the time required for image acquisition. Depending on the type of technique used, the time required for acquisition of images may be up to 45 minutes. [18]

1.1.2 Ventilation Imaging with PET

Positron emission tomography (PET) is a nuclear medicine technique that uses a radioactive isotope that is a positron emitter. The isotope is bound to a metabolically

active molecule. After the positron (antimatter electron) is emitted, it annihilates when it comes in contact with an electron. The annihilation process, which typically happens within 3 to 6 mm of lung tissue from the emission point, yields a pair of 511 keV photons that are ejected in opposite direction from one another. Gamma detectors, which are distributed in rings around the patient, are set to identify coincident photon pairs. Various computer algorithms are used to reconstruct the registered events into 3D image.

The most common radiopharmaceutical used for PET imaging is ^{18}F-fluorodeoxyglucose, more commonly known as FDG. This radiopharmaceutical incorporates a positron emitter (^{18}F) into a glucose analog. Tumors show preferential uptake of the sugar and the amount of concentration can often give information to distinguish malignant tumors from nonmalignant ones. Ventilation studies can be performed with intravenous fusion of $^{13}N_2$. [26, 43] During this procedure, the patient holds his or her breath for a short time while getting the injection. The concentration of the compound reaches a plateau. The washout phase starts when the patient resumes breathing and the concentration of the $^{13}N_2$ decreases with ventilation. Ventilation can be assessed using the washout data of $^{13}N_2$ since it is eliminated from the lung almost exclusively by ventilation.

1.1.3 Ventilation Imaging with MRI

Ventilation can also be quantified using magnetic resonance imaging (MRI). MRI is advantageous in imaging soft tissues such as brain or muscle. MRI images can be fused

with the images from the planning CT for radiation treatment to assist the radiation oncologist to better define tumor volumes. [44] MRI has two main advantages over other nuclear medicine ventilation imaging techniques because (1) it provides better spatial resolution, and (2) does not rely on ionizing radiation. There are various techniques to image ventilation with MRI, such as gadolinium based contrast agents, [45-47] oxygen enhancement, [48] and hyperpolarized ^{3}He and ^{129}Xe MRI. [49]

A common approach to MR ventilation imaging has been the use of gadolinium-based contrast agents such as aerosolized gadolinium chelates (Gd-DTPA). The issue with Gd-DTPA is the aerosol particle size (1-3 μm), which makes it susceptible to deposition in airwaves, in addition to the low signal-to-noise ratio. [45] The use of hyperpolarized noble gas requires specialized RF transmitter/receiver coils and laser equipment. Additionally, the gas is expensive and not yet suitable for routine clinical use, making this method costly and impractical. [28] Oxygen enhancement is a proton-based MR technique used for ventilation imaging. Despite the fact that oxygen is weakly paramagnetic, the effect of molecular oxygen on MRI is significant due to the large surface area of the lung. This method is more economical than hyperpolarized noble gas MR ventilation imaging. Oxygen enhancement drawbacks are its lower signal-to-noise ratio compared to hyperpolarized MR ventilation and its inability to capture dynamic changes in ventilation. [28, 37]

1.1.4 Ventilation Imaging with CT

Thoracic tumors frequently move with respiration. To account for this motion, many radiation oncologists order a 4D-CT scan at the time of CT simulation. Depending on the manufacturer either images are rapidly acquired then binned by respiratory phase or the raw sonogram data itself is binned according to respiratory phase. [50] A 4D-CT image set is comprised of complete CT image sets, each image set representing a particular point in the respiratory cycle.

Guerrero et al [31] suggested a pulmonary ventilation imaging algorithm, which would calculate the ventilation image for a 4D-CT image set. Deformable image registration (DIR) provides a point-to-point deformation matrix, and in this case is applied to determine the deformation from normal end expiration to normal end inspiration. Guerreo's method uses DIR and quantifies the density change within a particular voxel between the two end points of the respiratory cycle. The corresponding density changes (Hounsfield Unit changes) are used to calculate the local ventilation.

An algorithm presented by Zhang et al [37, 38] calculates the ventilation from the volume change (ΔV). The ΔV method is a direct geometrical calculation of the volume change. A specific volume change is obtained by applying the DIR transformation to each of the eight vertex positions of a voxel and then calculating the volume of the deformed volume element. Similarly, the algorithm presented by Reinhardt et al [30, 33, 34] derives ventilation by calculating the Jacobian of the deformation field to approximate the change in volume of voxels. Local volume change of the lung is calculated using the

Jacobian of the transformation that maps the end expiration phase of 4D-CT image to the end inspiration phase.

1.2 Deformable Image Registration

Image registration aligns image sets to establish correspondence between features in both sets. There are various forms of image registration that fall into two categories: rigid registration and deformable image registration. Rigid registration does not model changes from organ deformation due to breathing, patient weight loss, or tumor shrinkage, whereas deformable image registration (DIR) can take into account such changes. The goal of DIR is to find a transformation from one image set to another, such that the differences between the deformed and the target image sets are minimized by providing a voxel to voxel deformation matrix.

DIR has been studied since the early 1980s. For many years, neurosciences and neurosurgery have been the driving force for developing various deformation techniques. [51, 52] DIR is useful in many applications such as tumor motion estimation, [53] contour mapping, [54] dose mapping, [55] and more recently for calculation of ventilation. [29, 31-33, 36-38, 56, 57] Guerrero et al [53] used the optical flow (OF) method to map a delineated tumor from on CT image volume to the next on a point-by-point basis. Zhang et al [55] used the OF method to map dose to different phases of 4D-CT image to calculate more accurately the dose received by target volumes and surrounding organs. The OF method was also used

by Zhang et al[54] to map anatomic structures and tumor contours from one phase of the breathing cycle in a 4D-CT image set to different phases.

An application of DIR is image registration of two images from two different times during a breathing cycle (4D-CT). DIR finds a mapping between a voxel in one phase of the image (eg. end expiration) to a corresponding voxel in the second phase (eg. end inspiration). There are many deformable image registration algorithms that have been implemented. While the goal of these algorithms is the same, the algorithms are based on aligning different image features, how they measure similarity, and what type of deformations they allow. The algorithms described and evaluated in this paper are Optical Flow (OF), [54, 55, 58, 59] Diffeomorphic Demons (DD), [60-62] and Diffeomorphic Morphons (DM). [63]

Optical flow algorithm is based on two fundamental assumptions: (1) the intensity of a point in an image does not change with time and (2) the nearby points move in the same manner. This is known as the velocity smoothness constraint. It finds the voxel correspondence by computing a displacement field describing the apparent motion represented by the two images by matching the image intensity gradient. [54, 55, 59]

Diffeomorphic Morphons (DM) method is based on matching of edges and lines. [64] The Morphon iteratively deforms a moving image into a target image by morphing the moving image. The process can be divided into three parts: estimation of displacement, accumulation of the deformation field, and deformation. The estimation of displacement

has the aim to find the ways and indications on how to deform the moving image into the target image. The accumulation of the deformation field uses the estimate of the displacement to update the deformation field. Finally, the deformation morphs the moving image to the target image according to the accumulated deformation field. These steps are done iteratively as long as the displacement estimates indicate further morphing to be done.

The basis of the Diffeomorphic Demons (DD) method is matching of intensities. The main requirement is that the voxels in the moving image (*M*) have the same intensity as the corresponding voxels in the target image (*T*).[61, 62] Demons forces are applied on the moving image until there is an overlap in intensities between the two. The difference in intensity between the two ($M - T$) determines the applied force and its direction. When the difference between the two is greater than zero, *M* moves in the direction of $\vec{\nabla} T$, however, when the difference is less than zero *M* moves against $\vec{\nabla} T$. The demons stop exerting force when the images overlap completely.

For all deformable image registration algorithms, it is highly desirable to provide an estimate of the accuracy of their registration for the desired application. In this paper we have evaluated three DIR methods using an anatomical landmark based model, the POPI model [65, 66] and the image differences between the deformed and the target lung images. The model consists of anatomical landmarks in the lung chosen by expert radiologists. The intention of the model is to have landmarks that are spread uniformly and correspond to anatomical features such as the carina, calcified nodules, division

branch of the pulmonary artery, and apical pulmonary vein of the upper lobe and various bifurcations of smaller structures that could be uniquely identified in each image set. A complete description of the method is given by Sarrut et al [67] The POPI model is a useful tool that has been made available to researchers, which can be used to estimate the deformation accuracy in the lung.

The effect of the DIR on the ventilation algorithm is unknown, but if ventilation algorithms are robust then they will be insensitive to the precise DIR used provided the DIR is accurate. To test this hypothesis we investigated the dependence of calculated ventilation on the deformable image registration methods and on the ventilation algorithms.

This dissertation validates DIR methods used then compares ventilation images calculated from 4D-CT using DIR and ventilation algorithms (VA). The algorithms used for calculating ventilation are HU, ΔV, and the Jacobian. A total of nine combinations of methods (DIR and VA) are used to calculate ventilation images

CHAPTER 2 MATERIALS AND METHODS

We calculated lung ventilation from 4D-CT by using DIR and ventilation algorithms. We used three DIR algorithms (OF, DM, and DD) and three ventilation algorithms (HU, ΔV and Jacobian), to calculate ventilation images and then compared the similarities and differences between these images by using the Dice similarity coefficient index (DSC). In order to remove any registration errors, a $3\times3\times3$ mm^3 spatial averaging of all the resulting ventilation images was performed to generate the final ventilation image.

We validated the DIR algorithms using the datasets from the POPI model, which is a landmark based model used for validation of registration algorithms. [66] The DIR algorithms were then retrospectively applied to 20 patients, 10 esophageal and 10 lung cancer cases, all of which had associated 4D-CT image sets that encompassed the entire lung volume. We used the DSC index to quantify the similarities between the images generated with each method and to study the dependence of the ventilation images on the DIR and VA used. A total of 180 ventilation images, 9 for each case, were analyzed.

2.1 Deformable Image Registration

Deformable image registration (DIR) is a method for finding the mapping between each voxel in one phase of the image (eg. end exhale) and its corresponding deformed voxel (dvoxel) in another phase of the image (eg. end inhale) as illustrated in Figure 2. For example, in deforming a lung from end expiration to the corresponding lung at end inspiration the dvoxel will have a different volume from the original voxel. This is because the number of dvoxels in the inflated lung will be the same as the number of the original voxels in the un-inflated lung while the lung volume has increased.

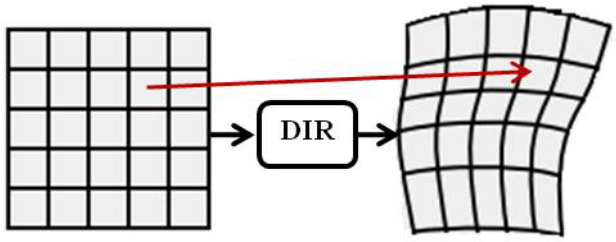

Figure 2. Deformable Image Registration. A voxel grid in the image on the left undergoes deformable image registration and is deformed like the grid on the right. The red arrow points to the corresponding deformed voxel on the right image.

During the deformable image registration process end expiration phase (moving image) is registered to the end inspiration phase (target image) and the result produces a deformation field. This deformation field is then entered into a ventilation algorithm that produces an image estimate of the ventilation, as illustrated in Figure 3.

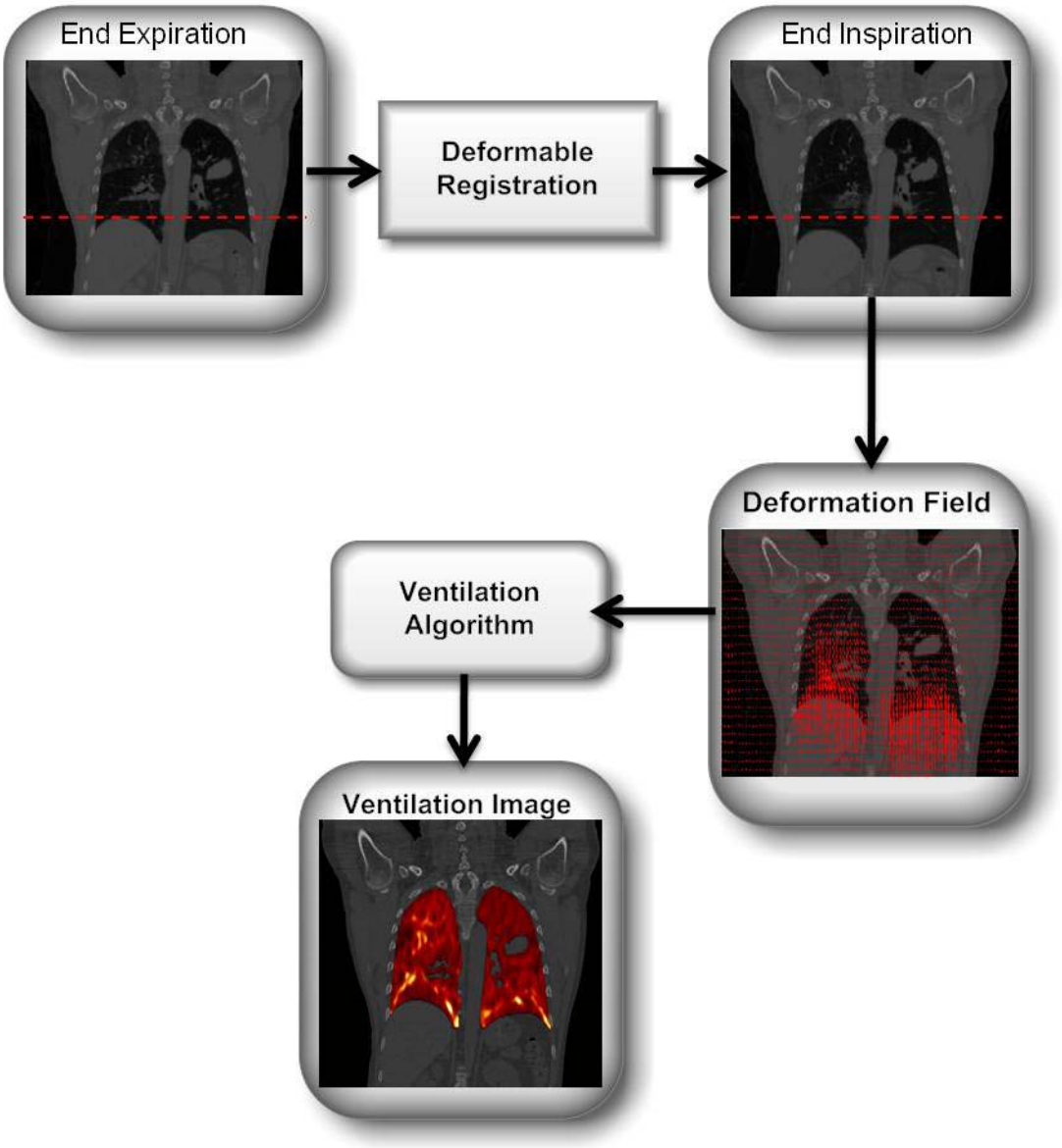

Figure 3. Illustration of the process of calculating ventilation images.

2.2 Deformable Image Registration Algorithms

Deformable image registration is used to find a point to point correspondence between two images. This maps the vertices of the original voxel to the vertices of the dvoxel. This correspondence describes the location of each voxel in one image relative to

the dvoxel in the second image. Three different registration algorithms, Optical Flow (OF), [53, 54, 58, 59] Diffeomorphic Morphons (DM) [64, 68], and Diffeomorphic Demons (DM), [62, 64, 69] were used to deform the end-expiration image (50%) to the end-inspiration (0%), mid-expiration (30%), and mid-inspiration image (70%).

2.2.1 Optical Flow

Optical flow finds the voxel correspondence by computing a displacement field describing the apparent motion represented by the two images by matching the image intensity gradient [54, 55, 59]. OF assumes that image intensity remains constant, intensity at time *t* is equal to the intensity at a later time $t+\delta t$, that is

$$I(\vec{x},t) \approx I(\vec{x}+\delta\vec{x},t+\delta t), \tag{1}$$

where $I(\vec{x},t)$ is the image intensity at time *t.* Taylor series expansion of the terms on the right-hand side of equation (1) yields:

$$I(\vec{x}+\delta\vec{x},t+\delta t) = I(\vec{x},t) + \vec{\nabla} I \cdot \delta\vec{x} + \delta t \frac{\partial I}{\partial t} + \ldots + \text{higher order terms} \tag{2}$$

Substitution of equation (2) into equation (1)yields:

$$I(\vec{x},t) = I(\vec{x},t) + \vec{\nabla} I \cdot \delta\vec{x} + \delta t \frac{\partial I}{\partial t} + \ldots + \text{higher order terms} \tag{3}$$

Ignoring the higher order terms in equation (3), and dividing by δt, we obtain the optical flow constraint equation:

$$\left(\vec{\nabla} I \cdot \vec{v} + \frac{\partial I}{\partial t}\right)(\vec{x},t) = 0, \tag{4}$$

where $\vec{v} = \frac{\partial \vec{x}}{\partial t}$ is the velocity and it consists of the displacement between a point in the first image, $I(\vec{x},t)$, and the corresponding point in the second image $I(\vec{x}+\delta\vec{x},t+\delta t)$ divided by the time between the two images, δt. For a single image pair the velocity matrix equals the displacement between the image volume pair. A velocity matrix is a complete collection of displacement vectors that relates every voxel from the source to the target image. A velocity constraint, which requires that nearby points move in a similar manner to each point, is introduced in order to obtain a single solution from equation (4) for each voxel. Finally, after allowing for small intensity variations and applying variational calculus the equation for the displacement field is obtained [53]:

$$\vec{v}_{n+1} = \vec{v}_n - \vec{\nabla} I \left(\frac{\vec{v}_n \cdot \vec{\nabla} I + \frac{\partial I}{\partial t}}{\alpha^2 + \left| \vec{\nabla} I \right|^2} \right), \tag{5}$$

where $\vec{v}$ is the displacement vector field, $I(\vec{x},t)$ is the intensity of the image, and the parameter α=1.4.

2.2.2 Diffeomorphic Demons

The basis of the Diffeomorphic Demons (DD) method is matching of gray levels. The Demons method is based on the thought experiment devised by Maxwell. In the experiment, a container is divided into two equal compartments, by an insulated wall in between, with a door that can be opened and closed by what came to be known as the "Maxwell's Demon." This demon opens the door to let only the high speed (hot)

molecules of gas to go through to one side of the compartment and closes the door otherwise. As a result, the temperature of one side gradually rises while the other side cools down, which violates the Second Law of Thermodynamics.

Maxwell's demon was adapted to a diffusion based method for deformable image registration by Thirion [61]. The main requirement, similar to the Optical Flow method, is that the voxels in the moving image have the same intensity as the corresponding voxels in the target image. Figure 4 is an illustration of the demons forces that are applied on the moving image until there is an overlap in intensities between the two. The gray image is the target (*T*) and the blue image is the moving image (*M*). The difference in intensity between the two (*M* – *T*) determines the applied force and its direction. When the difference between the two is greater than zero, *M* moves in the direction of $\vec{\nabla} T$, however, when the difference is less than zero *M* moves against $\vec{\nabla} T$. The demons stop exerting force when the images overlap completely. The force applied by the demons was inspired by the optical flow method but is renormalized because of the effects of small image intensity gradients.

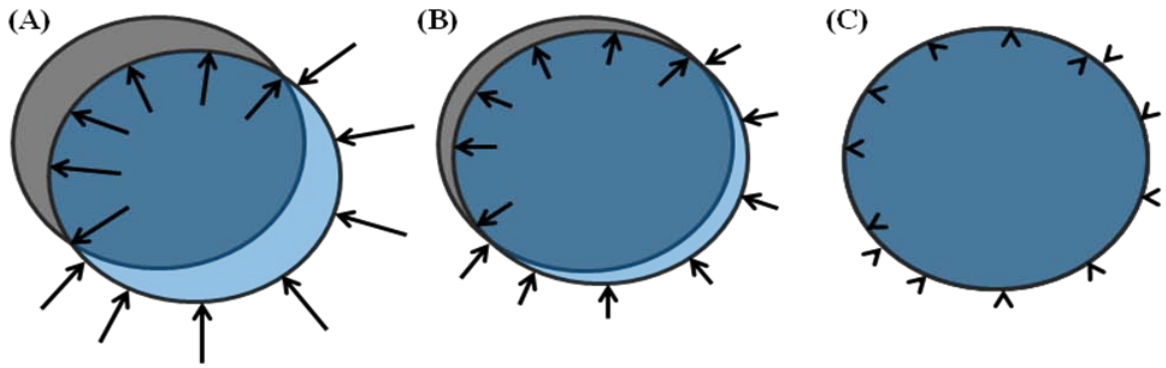

Figure 4. Demons forces. (A) In gray is the target image (*T*), transparent blue is the moving image (*M*). The demons indicated by vector arrows warp the image by applying a force in the direction of the image gradient. (B) There is a better overlap between the images, and as a result the corresponding force is reduced, indicated by shorter vectors. (C) The images overlap and there is no applied force by the demons because there is no difference in the gradient.

The resulting equation for the demons deformation field, as given by Thirion [61] is:

$$\vec{M}^{i}_{Update} = \frac{(M-T)\vec{\nabla}T}{\vec{\nabla}T^{2} + (M-T)^{2}}, \tag{6}$$

where $\vec{M}^{i}_{Update}$ is the update deformation field from the iteration *i*.

It was demonstrated by Vercauteren et al [60] that the deformation field given by equation (6) resembles an optimization of a second order gradient descent of the sum of the squared intensity differences (SSD). This indicates that Demons would function well in single modality registration, where SSD gradient descent is also appropriate, but it would not work well in multimodality registration where SSD is not appropriate. With this understanding, equation (6) is optimized in the form of symmetrical update rule:

$$\vec{M}^{i}_{Update} = \frac{(M - T)(\vec{\nabla}T + \vec{\nabla}M)}{\vec{\nabla}T^{2} + \vec{\nabla}M^{2}} \quad (7)$$

This optimization makes Demons more efficient and is the method that is implemented for our Demons registrations. Additionally, the Demons algorithm is updated to make it diffeomorphic. A diffeomorphism is a map between manifolds which is differentiable, and its inverse is differentiable as well. An advantage of diffeomorphic solutions is to prevent folding in the transformation. [62] As a result the Demons equation (**7**) is updated to:

$$\vec{M}^{i}_{Update} = \vec{M}^{i-1} + \exp(\vec{M}^{i}_{Update}) \quad (8)$$

This adaptation for accumulating the update field gives smoother deformation field when compared to the Demons method. The deformation field produced by the Diffeomorphic Demons (DD) is smoothed by a Gaussian, and iteratively used to transform the moving image, and register on to the static image. The DD uses a diffusion like Gaussian regularization of the displacement field which leads to smooth fields. Regularization is applied to reduce the influence of extreme values in a deformation field.

2.2.3 Diffeomorphic Morphons

Diffeomorphic Morphons (DM) method is based on matching of edges and lines. [64] The Morphon iteratively deforms a moving image into a target image by morphing the

moving image. The process can be divided into three parts: estimation of displacement, accumulation of the deformation field, and deformation.

The estimation of displacement has the aim to find the ways and indications on how to deform the moving image into the target image. Estimation of displacement is based on quadrature phase difference. The accumulation of the deformation field uses the estimate of the displacement to update the deformation field. This process is done in two steps: the first step is the update of the deformation field and then regularization of the estimates of the accumulated field in order to fit the observed deformation to a deformation model. Finally, the deformation morphs the moving image to the target image according to the accumulated deformation field. These steps are done iteratively as long as the displacement estimates indicate further morphing to be done.

Quadrature phase difference is a method used to estimate local displacement between two images. The advantage of this method over other methods, such as the ones based on gradient and polynomial expansion, is its invariance to image intensity and weak gradients. [63] Quadrature phase is a measure of local structure. Edges between bright and dark areas have one phase, dark lines have one phase, and lines on dark background have a phase as well as bright patches. The transition as we move from one phase to another is continuous. Therefore, the difference in local phase between the moving and target images is a good measure of how much the moving image has to move to fit the target image. The local displacement is a function of the local phase along its associated direction. To estimate the local displacement a least square estimate is used.

$$\min_{\mathbf{v}} \sum_i \left[w_i (\hat{n}_i^T \mathbf{v} - v_i) \right]^2, \tag{9}$$

where $\mathbf{v}$ is the displacement field estimate, v_i is the displacement field associated to the filter direction *i*, w_i is a measure of certainty and it is derived from the magnitude of the phase difference, and $\hat{\mathbf{n}}_i$ is the direction of the filter *i*.

The displacement field of the current iteration is given by equation (9) , which is used to interpolate a deformed version of the moving image. The moving image is deformed based on the accumulated field and then it is compared to the target image in order to estimate a displacement field for the current iteration being performed. The updated field ($\mathbf{d}_a^{'}$) is formed by combining the accumulated field ($\mathbf{d}_a$) and the displacement field from the current iteration ($\mathbf{d}_k$).

$$\mathbf{d}_a^{'} = \frac{\mathbf{d}_a c_a + (\mathbf{d}_a + \mathbf{d}_k) c_k}{c_a + c_k} \ , \tag{10}$$

where c_a and c_k are the uncertainties in the accumulated field and the temporary field respectively. After acquiring the update field in equation (10) as well as the certainty from the field, a weighted accumulation is used to determine the accumulated displacement field:

$$\vec{\mathbf{d}}^i = \vec{\mathbf{d}}^{i-1} + \frac{c_U \mathbf{d}_a^{'}}{c^{i-1} + c_U}, \tag{11}$$

where c_U is the uncertainty in the update field.

Similar to the Demons method, the Morphons method is optimized to become diffeomorphic. As a result, equation (11) becomes:

$$\vec{\mathbf{d}}^{i} = \vec{\mathbf{d}}^{i-1} + \exp\left(\frac{c_U \mathbf{d}'_a}{c^{i-1} + c_U} \right) \tag{12}$$

As in the DD method, the deformation field produced by the DM is smoothed by a Gaussian, and iteratively used to transform the moving image, and register on to the static image. The DM uses a diffusion like Gaussian regularization of the displacement field which leads to smooth fields. Regularization is applied to reduce the influence of extreme values in a deformation field.

All three DIR methods are implemented in an iterative and multiscale scheme. A lower resolution deformation is first approximated then used for the next level of deformations with a higher resolution of the images to be registered. This process continues until the deformation has been approximated at the highest resolution.

Four scales of resolution were used when using OF, with 98 iterations at each scale. DD and DM were applied using the settings described in Janssens et al, that is using eight scales, with a maximum of 20 iterations at each scale and a smoothing standard deviation of 2. [64]

2.3 Implementation of the DIR Methods

All three DIR methods are implemented in an iterative and multi-scale scheme. A lower resolution deformation is first approximated then used for the next level of

deformations with a higher resolution of the images to be registered. This process continues until the deformation has been approximated at the highest resolution. OF is implemented using C++ with four scales of resolution, and 98 iterations at each scale, which was determined to be the optimal number of iterations for OF. DD and DM were implemented using MATLAB[4]. The settings were the same as the ones described in Janssens et al. that is using eight scales, with a minimum of 10 and a maximum of 20 iterations at each scale and a smoothing standard deviation of 2. The iterative process was stopped if the changes measured in terms of the sum of the squared differenceses (SSD) were less than 0.01%. [64]

2.4 Validation of Deformable Image Registration Algorithms

All three DIR algorithms were evaluated using the POPI model. The POPI model consists of a 4D-CT image data set of a lung with the images binned into 10 phases along with 41 associated anatomical landmarks. The landmarks are anatomically homologous points that were manually delineated by radiologists at all 10 phases of the original 4D-CT image sets. [66] A projection of the points on the CT planes is shown in Figure 5. They are based on anatomical features that correspond to various locations in the lung, such as the carina, calcified nodules, culmen-lingula junction, division branch of pulmonary artery, and apical pulmonary vein of the upper lobe. [67] the CT image sets consisted of 512×512×141 voxels with voxel dimensions of 0.97×0.97×2mm^3 (2 mm slice thickness).

[4] MATLAB® is a registered trademark of The MathWorks, Inc. 3 Apple Hill Drive Natick, MA 01760 USA. (www.mathworks.com)

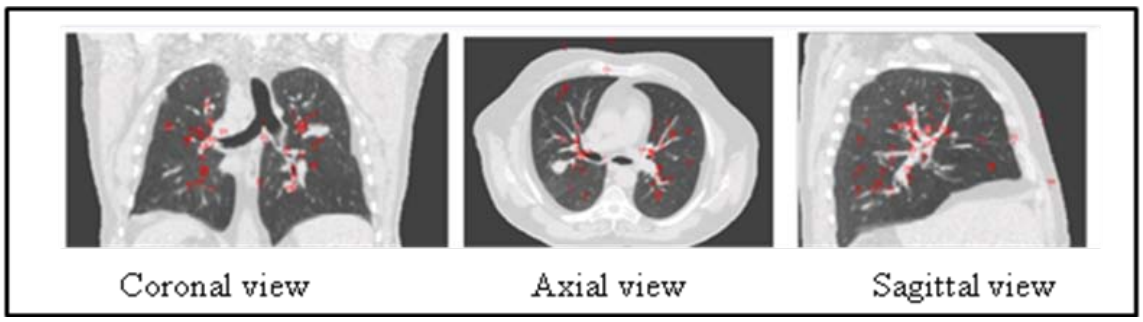

Figure 5. Projections of the landmarks on the three body planes. Images courtesy of the Léon Bérard Cancer Center & CREATIS lab, Lyon, France.

The phases used for the evaluation of the DIR algorithms were normal end-inspiration (0% phase), mid-expiration (30% phase, the phase that lies between the end-inspiration and end-expiration) normal end-expiration (50% phase), and the 70% phase which is mid inspiration or the phase that lies between the end-expiration and end-inspiration[5] For all the methods, the original data sets were used for this validation without any resampling.

Using deformable registration one phase is registered to the second phase (eg. end-expiration to end-inspiration phase). This generates deformation vector fields (DVFs) that approximate the anatomical displacements voxel-by-voxel. The vector fields point from the target positions to the where the displaced new positions of the anatomical features. For this study the 0%, 30% and 70% phases were each registered to the 50% phase.

[5] The model and landmarks were provided for use by the group at Léon Bérard Cancer Center & CREATIS lab, Lyon, France.

The resulting deformation fields were used to calculate the new location of the landmarks on the end expiration phase. Then the positions of the calculated landmarks were compared to the inspiration phase landmarks as determined by the radiologists. Target registration error (TRE) was calculated by calculating the displacement between the calculated and the anatomically determined landmarks for each of the radiologist identified points. This displacement was used as the metric to assess the accuracy of the registration algorithms.

Additionally, the DIR algorithms were evaluated on a voxel-to-voxel basis by calculating the differences between the deformed image and the target image. The image calculator feature of ImageJ 1.44n (National Institutes of Health) was used to calculate the differences in Houndsfield Units (HU) between the two images. The difference in HU between the deformed and target images is used as an indicator of the accuracy of the registration. A region of interest (ROI) was drawn to only include the voxels inside the lung and exclude the rest of the image. For comparison, the differences between the moving and the target images were calculated without using any deformable registration (NO DIR).

2.5 Ventilation Methods

2.5.1 Jacobian Ventilation

The Jacobian method is a mathematical representation of volume change that uses the first derivative of the deformation field to approximate the change in volume of voxels. [29, 30, 33, 34] Local volume change of the lung is calculated using the Jacobian of the transformation that maps the end expiration phase of 4D-CT image to the end inspiration phase. Consider a function that represents a vector displacement $\boldsymbol{D}(x,y,z)$ that transforms a voxel from its end expiration image to its corresponding location in the end inspiration image, so that the voxel at (x,y,z) in the end expiration image is displaced by a vector $\boldsymbol{D}(x,y,z)$ to map it to its corresponding location in the end inspiration image. The Jacobian J of this transformation is:

$$J = \det\left[I + \begin{pmatrix} \frac{\partial D_x(x,y,z)}{\partial x} & \frac{\partial D_x(x,y,z)}{\partial y} & \frac{\partial D_x(x,y,z)}{\partial z} \\ \frac{\partial D_y(x,y,z)}{\partial x} & \frac{\partial D_y(x,y,z)}{\partial y} & \frac{\partial D_y(x,y,z)}{\partial z} \\ \frac{\partial D_z(x,y,z)}{\partial x} & \frac{\partial D_z(x,y,z)}{\partial y} & \frac{\partial D_z(x,y,z)}{\partial z} \end{pmatrix} \right], \tag{13}$$

where I is the identity matrix, $D_x(x,y,z)$ is the x component of $\boldsymbol{D}(x,y,z)$, $D_y(x,y,z)$ is the y component of $\boldsymbol{D}(x,y,z)$, and $D_z(x,y,z)$ is the z component of $\boldsymbol{D}(x,y,z)$. The Jacobian operator is used to extract volume changes on a voxel level directly from the deformation field. The determinant of the Jacobian is calculated at each voxel position according to equation (13). If the determinant of the Jacobian is unity then no expansion or contraction

in the function $\boldsymbol{D}(x,y,z)$. If the determinant is greater than one, there is local tissue expansion, if less than one, there is local tissue contraction.

2.5.2 ΔV Ventilation

The ΔV method is a direct geometrical calculation of the volume change [70]. Each cuboid volume in a CT is composed by 8 neighboring voxels as vertices. This cuboid can be used to represent the volume of the voxel. These vertices, as seen in image 1 of Figure 6, are changed to create a 12-face polyhedron in image 2. The polyhedron is still comprised by the 8 vertices, however, it is now deformed and the correspondence between the deformed vertices and the original ones is established by deformable image registration. The cuboid and the polyhedron are comprised of 6 tetrahedrons, as seen in Figure 7(A) and (B). The volumes of the cuboid and the deformed polyhedron are the sums of the volumes of their corresponding tetrahedrons. During the local volume change calculation, the volume of each voxel is calculated using the corresponding vertices of each respective polyhedron.

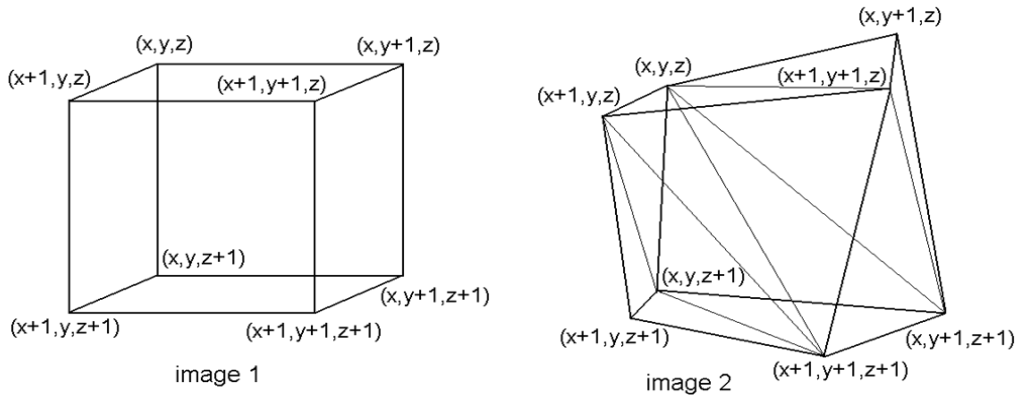

Figure 6. A cuboid in image 1 that represents a voxel (x,y,x) deforms to a 12-face polyhedron in image 2. Both images have 8 vertices, which define the same local volume at different respiratory phases. Used with permission. [38]

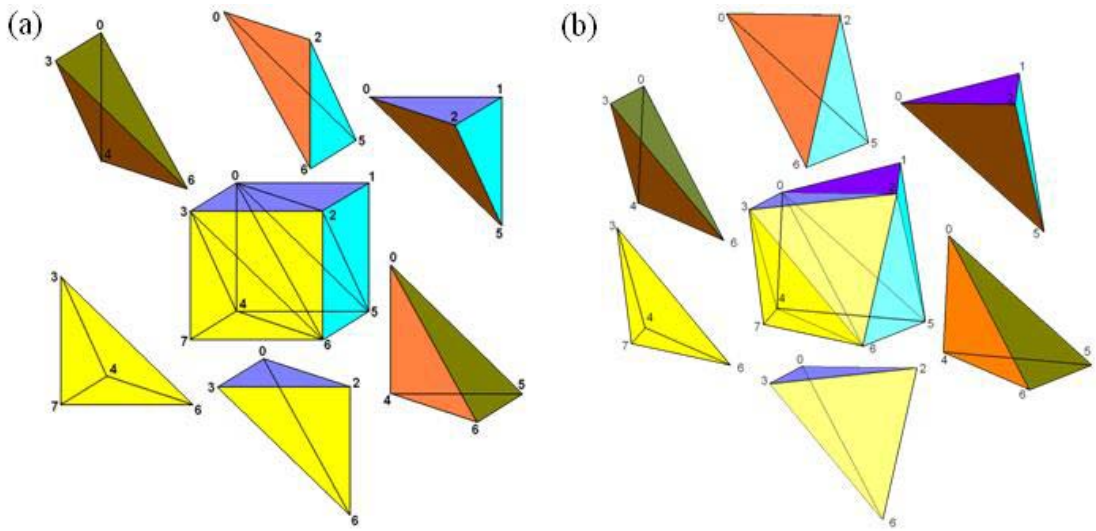

Figure 7. (a) A cuboid can be divided in 6 tetrahedrons. (b) The deformed cuboid, now a polyhedron, is composed of 6 deformed tetrahedrons. Used with permission. [38]

The fundamental volume calculation derives from calculating the volume of each tetrahedron. The volume of tetrahedron is calculated by using the coordinates of its 4 vertices:

$$V = (\vec{b} - \vec{a}) \cdot [(\vec{c} - \vec{a}) \times (\vec{d} - \vec{a})] / 6, \tag{14}$$

where $\vec{a}, \vec{b}, \vec{c}, \vec{d}$ are the vertices of the tetrahedron as vectors. The volume of a given polyhedron is calculated by summing the volumes of the six tetrahedrons. The coordinates of the deformed tetrahedron are given by the deformation matrix, which is derived from the DIR of the original voxel.

2.5.3 HU Ventilation

The HU method uses deformable image registration to correlate voxels from the expiration image set to the anatomically corresponding dvoxels in the inspiration image. Then the change in density is calculated by direct comparison of Houndsfield Units (HUs) [32, 35].

$$F_{air} = -\frac{HU}{1000} \tag{15}$$

$$\frac{\Delta V}{V_{ex}} = \frac{F_2 - F_1}{F_1(1 - F_2)} \tag{16}$$

Let F_1 be the fraction of air in the exhale CT volume, and F_2 the fraction of air in the inhale CT volume:

$$\frac{\Delta V}{V_{ex}} = \frac{F_{in} - F_{exh}}{F_{exh}(1 - F_{in})} \tag{17}$$

Substitute equation (15) in to equation (17):

$$\frac{\Delta V}{V_{ex}} = \frac{-\frac{HU_{in}}{1000} + \frac{HU_{exh}}{1000}}{-\frac{HU_{exh}}{1000}(1 + \frac{HU_{in}}{1000})} \tag{18}$$

Simplifying further we get to the final equation:

$$\frac{\Delta V}{V_{ex}} = 1000 \frac{(HU_{in} - HU_{exh})}{HU_{exh}(1000 + HU_{in})} \tag{19}$$

2.6 Cases

Twenty patients, ten lung and ten esophageal cancer patients, treated using external beam radiotherapy were selected for the retrospective study. The patients and 4D-CT image characteristics of the 20 cases utilized in this study are given in Table 1. Free breathing 4D-CT image sets were collected on a Philips Large Bore Brilliance 16 slice scanner (Philips Oncology Systems, Cleveland Ohio). The CT sinogram data were binned into 10 phases based on bellows on the abdomen using the method described by Keall et al. [71]

Table 1. Ventilation cases. The patient data included in this study are summarized.

Case number	Malignancy	4D-CT image dimension	4D-CT voxel dimension (mm)
1	Eso ca.	512×512×137	0.976×0.976×3
2	Eso ca.	512×512×128	0.976×0.976×3
3	Eso ca.	512×512×107	0.976×0.976×3
4	Eso ca.	512×512×130	1.17×1.17×3
5	Eso ca.	512×512×114	1.17×1.17×3
6	Eso ca.	512×512×129	1.17×1.17×3
7	Eso ca.	512×512×130	1.17×1.17×3
8	Eso ca.	512×512×106	1.17×1.17×3
9	Eso ca.	512×512×115	1.17×1.17×3
10	Eso ca.	512×512×123	1.17×1.17×3
11	NSCLC	512×512×145	1.17×1.17×3
12	SCLC	512×512×125	0.976×0.976×3
13	NSCLC	512×512×107	0.976×0.976×3
14	NSCLC	512×512×110	0.976×0.976×3
15	SCLC	512×512×145	1.17×1.17×3
16	SCLC	512×512×118	1.17×1.17×3
17	NSCLC	512×512×145	1.17×1.17×3
18	NSCLC	512×512×128	0.976×0.976×3
19	SCLC	512×512×127	1.17×1.17×3
20	SCLC	512×512×122	1.17×1.17×3

Abbreviations: Eso ca. = esophagus cancer; NSCLC = non-small cell lung cancer; SCLC = small cell lung cancer.

2.7 Image Analysis

2.7.1 Ventilation Dependence on the DIR

We compared ventilation images calculated with the three DIR methods by calculating the DSC index between images that were calculated with the same ventilation algorithm but different DIR method, as illustrated in Figure 8. The process was repeated for images calculated with the second, and then the third ventilation algorithm. This analysis was done for all 20 cases.

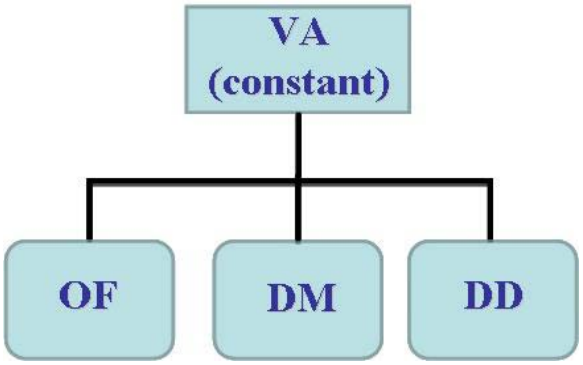

Figure 8. Schematic illustration representing the study of ventilation dependence on the DIR algorithm used.

2.7.2 Ventilation Dependence on the Ventilation Algorithm

To calculate ventilation dependence on the ventilation algorithm (VA), images calculated with the three different VAs, but same DIR, were compared to each other via the DSC index then repeating the process for images calculated with the second and third DIR method. The process is illustrated with a schematic shown in Figure 9.

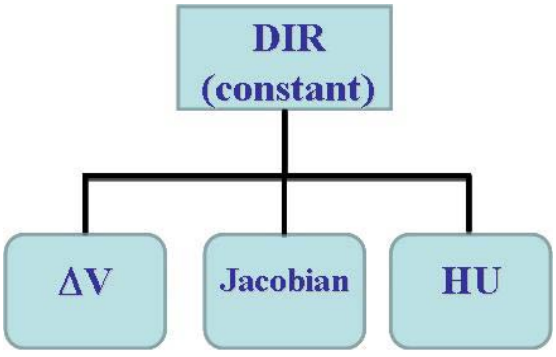

Figure 9. Schematic illustration representing the study of ventilation dependence on the ventilation algorithm used.

2.7.3 Retrospective Image Analysis

4D-CT sets from twenty patients, ten lung and ten esophageal cancer patients, treated with external beam radiotherapy were selected for the retrospective study. 4D-CT image sets were collected on a Philips Large Bore Brilliance 16 slice scanner (Philips Oncology Systems, Cleveland Ohio). The CT sinogram data were binned into 10 phases based on bellows on the abdomen using the method described by Keall et al. [71] The pixel size of the 4D-CT images, for thirteen cases, was approximately 1.17×1.17×3 mm^3 (3 mm slice thickness). Seven had a pixel size of 0.976×0.976×3 mm^3 in the transaxial slice of the 4D-CT images.

2.7.4 Dice Similarity Coefficient (DSC)

Dice similarity coefficient analysis was performed on the ventilation images [72, 73]. Overlap between the two volumes was assessed with the Dice similarity coefficient index. DSC index is a measure of the degree of overlap between two areas or volumes. For a reference volume *A* and a volume *B* to be compared to the reference Dice similarity coefficient is:

$$DSC(A,B) = \frac{2 \times |A \cap B|}{|A| + |B|} \tag{20}$$

DSC is defined as twice the shared information (intersection) over the sum of the two volumes. The DSC index is a measure of the amount of association between two methods compared. The values of DSC index range from 1.0 and 0.0. A DSC index of 1.0 indicates a complete overlap of the two methods examined whereas a DSC index of 0.0 indicates no overlap between the methods examined, and intermediate values give proportional amount of overlap.

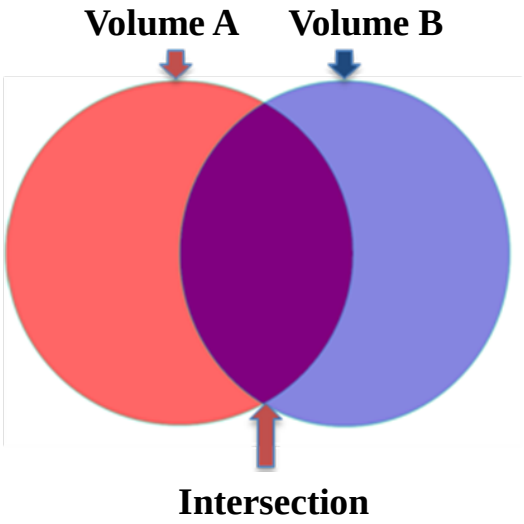

Figure 10. Dice similarity coefficient.

A threshold of lower and upper 20% ventilation was used to compare images to eachother. Thresholded volumes with their respective ventilation values were created for each image and then compared to each other. That is the lower 20% ventilation in one image was compared to the lower 20% ventilation in the second image. The overlap, or the similarity between the two volumes was calculated using the DSC index. Additionally, the images that were thresholded with the upper 20% ventilation were compared using the DSC index.

2.7.5 Ventilation Image Differences

Differences between the ventilation images generated by the ΔV method using OF, DM and DD registration were examined using image to image differences. Additionally, differences between the ventilation images generated by the Jacobian, ΔV, and HU methods using OF registration were examined using image to image differences. Image B was subtracted from image A which resulted in image C. A histogram, as well as the mean and standard deviation of the image C were calculated

CHAPTER 3 RESULTS

3.1 Validation of Deformable Image Registration Algorithms

Only 39 of 41 landmarks in the POPI model were used. Two of the landmarks were intentionally not used for the evaluation because one of them was outside the area of interest and the other one corresponded to a 4D-CT artifact. Table 1, Table 2, and Table 3 show a summary of the statistics of target registration errors for the OF, DM, and DD algorithms. Without DIR, the average landmark distance between the end-expiration and end-inspiration (50% and 0%) phases was 5.7±2.5 mm, with a range of 0.6 to 12.0 mm. The average TRE for the DIR algorithms for the 50% to 0% registration were 1.6±0.9 mm, with a range of 0.2 to 3.7 mm for OF, 1.4±0.6 mm, with a range of 0.2 to 3.3 mm for DM, 1.4±0.7 mm, with a range of 0.3 to 3.3 mm for DD, indicating registration errors were within 2 voxels. The average TRE for the 50% to 30% deformable registration were 1.9±1.7 mm, with a range of 0.4 to 6.3 mm for OF, 1.3±0.7 mm, with a range of 0.2 to 3.8 mm for DM, 1.3±0.7 mm, with a range of 0.2 to 3.1 mm for DD, indicating registration errors were within 2 voxels. The average landmark distance between the 50% and 30% phases was 3.8±2.2 mm, with a range of 0.3 to 10.0 mm.

The average TRE for the 50% to 70% deformable registration were 0.9±0.7 mm, with a range of 0.1 to 3.3 mm for OF, 1.2±0.5 mm, with a range of 0.1 to 2.7 mm for DM, 0.7±0.4 mm, with a range of 0.1 to 2.1 mm for DD, indicating registration errors were within 2 voxels. The average landmark difference between the 50% and 70% phases without any registration was 1.8±1.1 mm, with a range of 0.3 to 4.3 mm. One way analysis of variance (ANOVA) was used to assess the differences between the three DIR methods. The differences between the TREs using OF, DM, and DD were not significant, p-value of 0.37.

Table 2. Summary of the magnitude of the target registration errors for the three deformable image registration methods, for 50%-30%, and the distances between landmarks without registration (NO DIR).

phases	50%-30%			
	OF	DM	DD	NO DIR
Mean (mm)	1.9	1.3	1.3	3.8
SD (mm)	1.7	0.7	0.7	2.2
Max (mm)	6.3	3.8	3.1	10
Min (mm)	0.4	0.2	0.2	0.3

Table 3. Summary of the magnitude of the target registration errors for the three deformable image registration methods, for 50%-30%, and the distances between landmarks without registration (NO DIR).

phases	**50%-30%**			
	OF	DM	DD	NO DIR
Mean (mm)	1.9	1.3	1.3	3.8
SD (mm)	1.7	0.7	0.7	2.2
Max (mm)	6.3	3.8	3.1	10
Min (mm)	0.4	0.2	0.2	0.3

Table 4. Summary of the magnitude of the target registration errors for the three deformable image registration methods, for 50%-70%, and the distances between landmarks without registration (NO DIR).

phases	**50%-70%**			
	OF	DM	DD	NO DIR
Mean (mm)	0.9	1.2	0.7	1.8
SD (mm)	0.7	0.5	0.4	1.1
Max (mm)	3.3	2.7	2.1	4.3
Min (mm)	0.1	0.1	0.1	0.3

Figures 11−14 show TRE plots of the 0%-50 % registration for each point, and the dashed lines in these figures represent a +/- two voxel error. Figure 11 (a) shows a plot of TRE in the anterior-posterior (AP) direction for the three DIR algorithms (OF, DM, and DD), and Figure 11 (b) shows the distance between the phases of landmarks in

the AP without any registration (NO DIR). Figure 12 (a) shows a plot of TRE in the lateral (LAT) direction for the three DIR algorithms, and Figure 12 (b) shows the distance between the phases of landmarks in the LAT without any registration. Figure 13 (a) shows a plot of TRE in the superior-inferior (SI) direction for the three DIR algorithms, and Figure 13 (b), shows the distance between the phases of landmarks in the SI without any registration. Figure 14 (a) shows the magnitude of the TRE for DIR and Figure 14 (b) shows the magnitude of landmark distance without DIR.

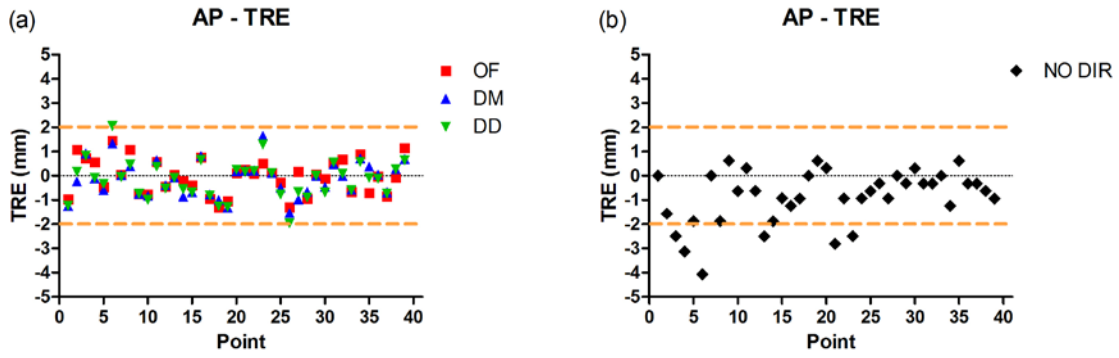

Figure 11. (a) Target registration errors (TRE) of the 3 DIR methods in the anterior-posterior (AP) direction. The maximum TRE for all three DIRs was less than two voxels, marked with the dashed lines. (b) The distance in AP between the landmarks without any registration.

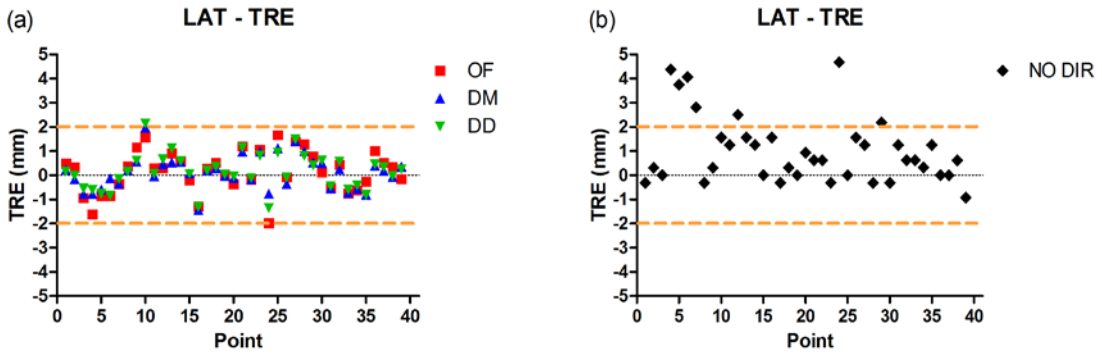

Figure 12. (a) Target registration error in the lateral direction. All three DIR methods performed similarly and had target registration error within two voxels shown by the two dashed lines. (b) The distance in lateral between the landmarks without any registration.

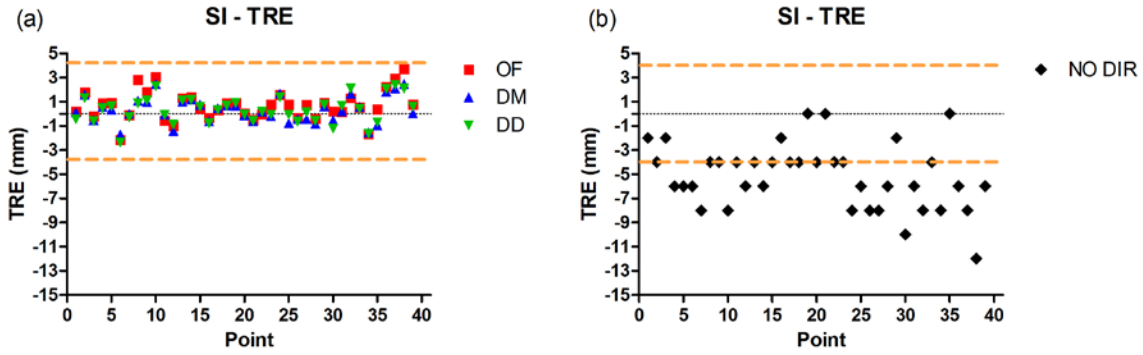

Figure 13. (a) Target registration error in the superior-inferior (SI) direction. The target registration errors were within two voxels shown by the two dashed lines. (b) The distance in SI direction between the landmarks without any registration.

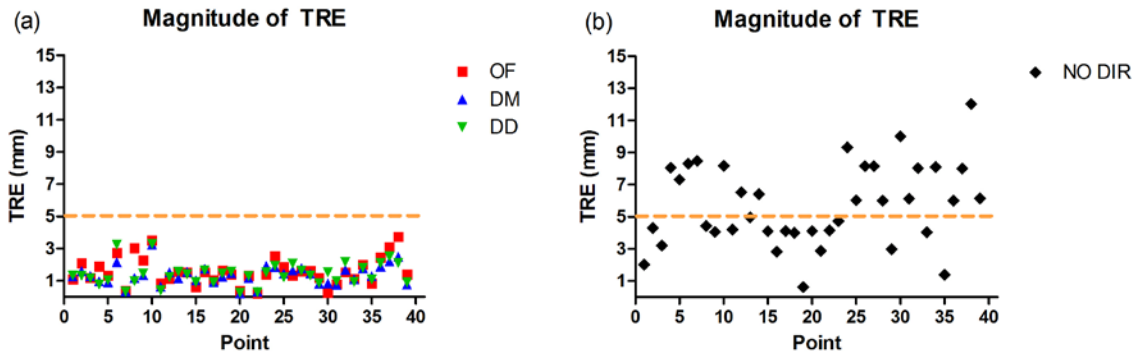

Figure 14. (a) The magnitude of target registration errors for the DIR methods. The maximum TRE for all three methods was within two voxels as denoted by the dashed line. OF mean TRE = 1.6±0.9 mm, DM mean TRE = 1.4±0.6 mm, and DD mean TRE = 1.4±0.7 mm. (b) The distances between the landmarks without any registration. The mean landmark distance with NO DIR was 5.7±2.5 mm.

Image difference is another validation method for the DIR algorithms to determine the degree of accuracy of deformable registration. Figure 15 shows a representative slice of the image difference for the three DIR methods and the differences between the two image phases without any registration (NO DIR). For the OF algorithm 81% of voxels were within a difference of 50 HU, and 93% of the voxels were within 100 HU. For the DM algorithm 69% of voxels were within 50 HU, and 87% within 100 HU. For the DD algorithm 71% of the voxels were within 50 HU, and 87% within a difference of 100 HU. The image differences without deformable image registration (NO DIR) between the moving and the target images were 50% within 50 HU, and 69% within 100 HU. Figure 16 displays a histogram of the differences between the target and the deformed images as a percentage of the total voxels for all the algorithms as well as the

difference between the target and the moving images without a DIR to set a baseline. Overall differences between the DIR methods are small.

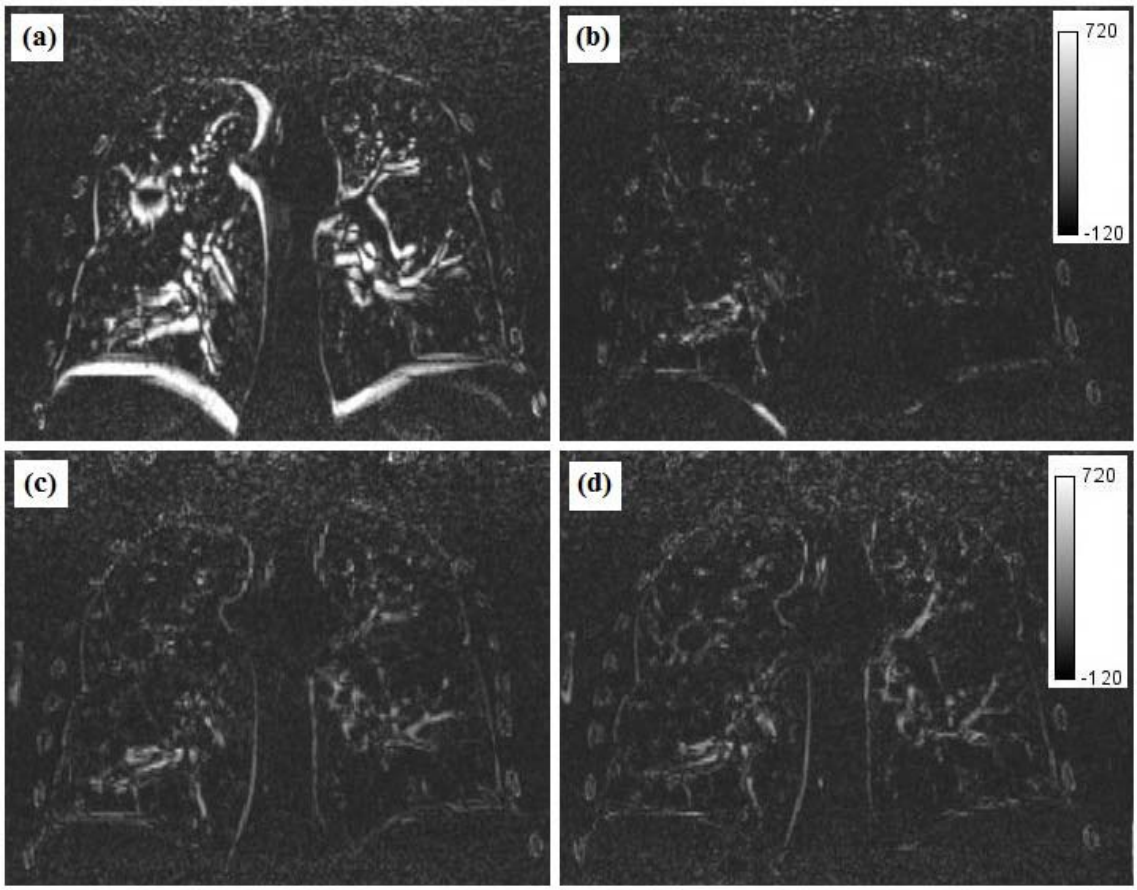

Figure 15. Image differences between the deformed and the target images for (a) NO DIR, (b) Optical Flow, (c) Diffeomorphic Morphons, and (d) Diffeomorphic Demons.

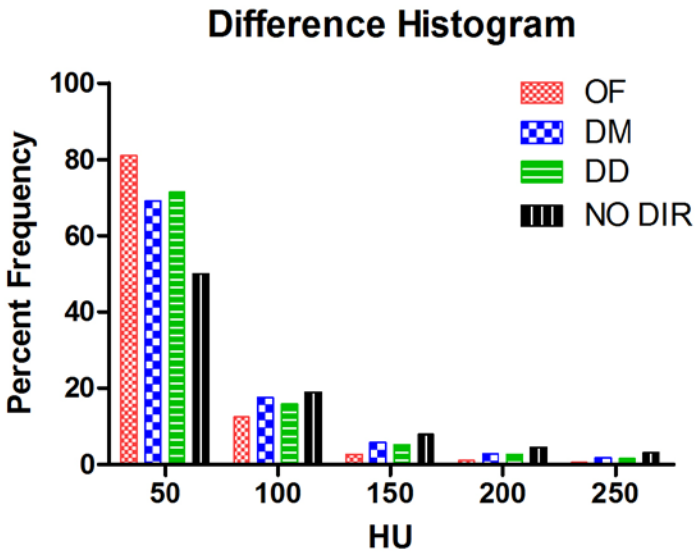

Figure 16. Histogram of the differences between the deformed and the target images. The histogram shows the differences in HU between the images as a percentage of the total number of voxels encompassed by the region of interest. The NO DIR shows the HU difference between the moving and the target images.

3.2 Ventilation Dependence on the DIR

Figure 17 (a), (b), and (c) show coronal and axial images of the calculated ventilation using the ΔV ventilation method with the OF, DM, and DD deformable image registration algorithms. Bright colors in the images show high ventilation and dark colors show low ventilation regions. The high ventilation areas seem to correspond between the different methods, but the overall images are quite different from each other.

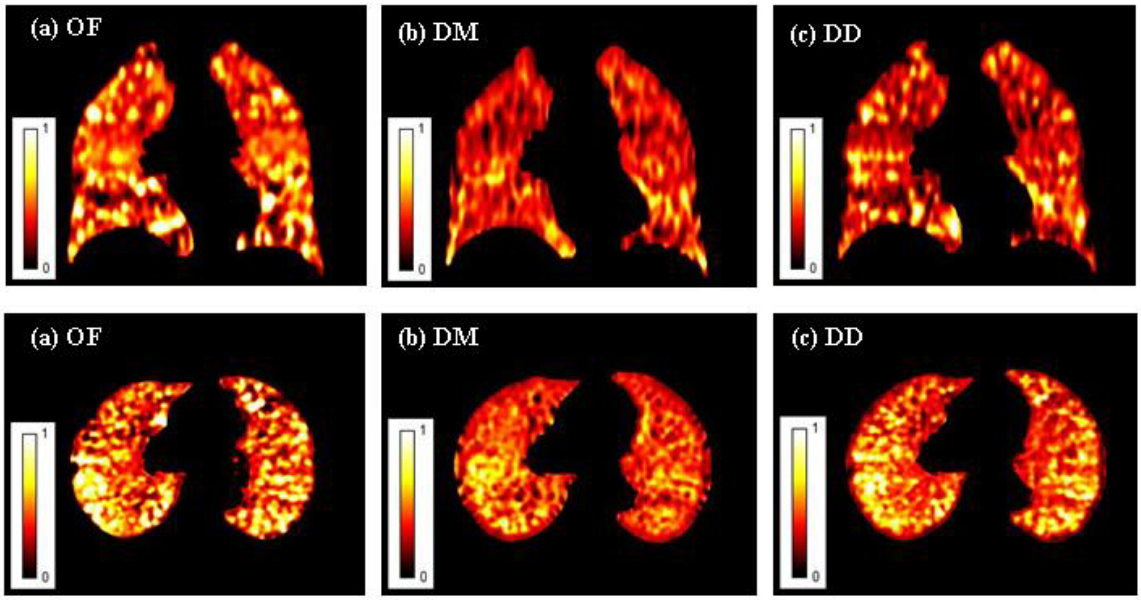

Figure 17. Coronal and axial slices of the ΔV ventilation images for a representative patient with (a) OF, (b) DM and (c) DD deformation.

Figure 18 (a), (b), and (c) show coronal and axial images of the calculated ventilation using the Jacobian ventilation method with the OF, DM, and DD deformable image registration algorithms. A visual inspection shows that the images in A and C have a good correspondence between the high and low ventilation areas; however, the image in B seems to be quite different from the other two.

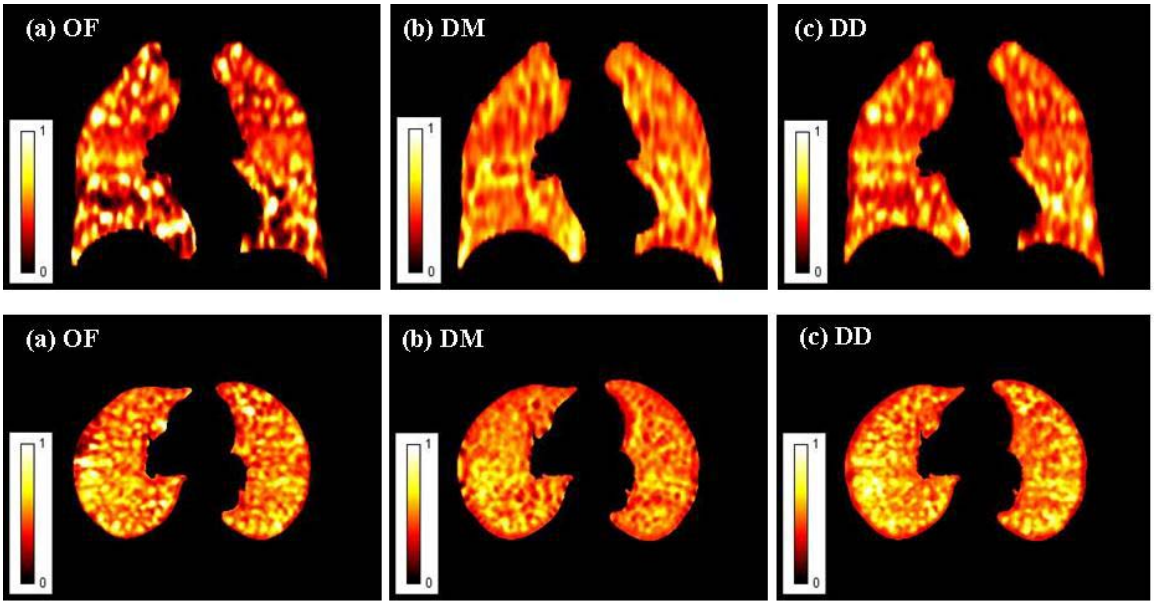

Figure 18. Coronal and axial images of Jacobian ventilation images with OF (a), DM (b) and DD (c) deformation.

Figure 19 (a), (b), and (c) show coronal and axial images of the calculated ventilation using the HU ventilation method with the OF, DM, and DD deformable image registration algorithms.

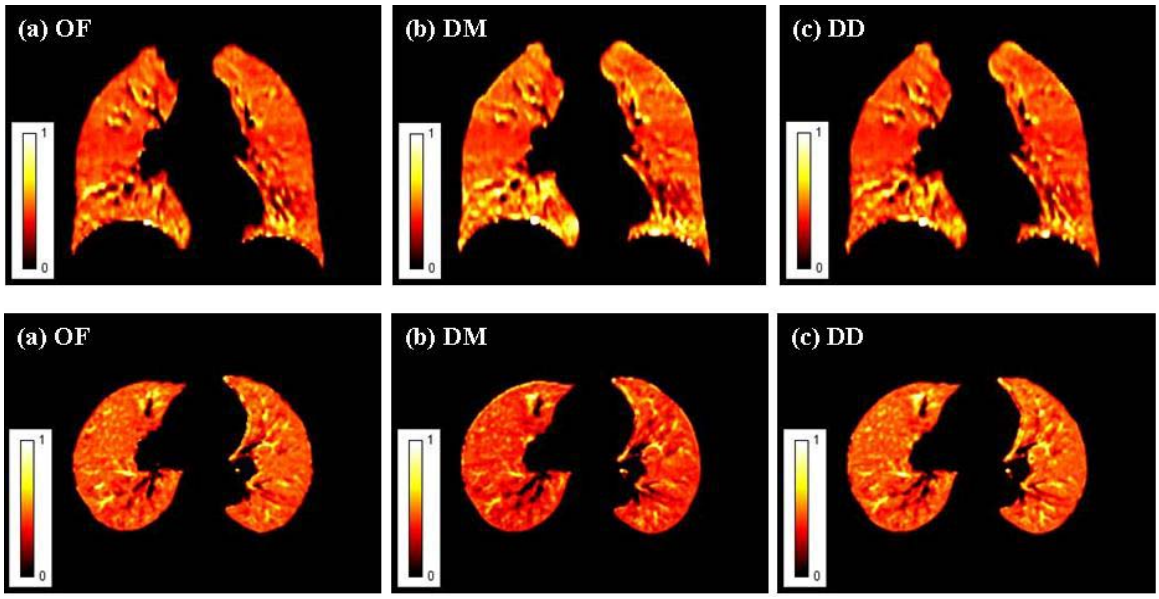

Figure 19. Coronal and axial images of HU ventilation with OF (a), DM (b) and DD (c) deformation.

Table 5 shows a statistical summary of the DSC index in the (0-20)% percentile range for all 20 patients comparing the ΔV, Jacobian, and HU ventilation calculated using the OF, DM, and DD deformation algorithms. DSC for 20% of low ventilation volume for ΔV was 0.33 ± 0.03 between OF and DM, 0.44 ± 0.05 between OF and DD and 0.51 ± 0.04 between DM and DD. The similarity comparisons for Jacobian was 0.32 ± 0.03, 0.44 ± 0.05 and 0.51 ± 0.04 respectively, and for HU 0.53 ± 0.03, 0.56 ± 0.03 and 0.76 ± 0.04 respectively. As presented in Table 6, DSC for the (80-100)% percentile ventilation showed trends similar to the lower ventilation.

Table 5. Dice similarity coefficient between deformation pairs for the lowest (0-20)% ventilation.

Vent.	**ΔV**			**Jacobian**			**HU**		
DIR	OF DM	OF DD	DM DD	OF DM	OF DD	DM DD	OF DM	OF DD	DM DD
Mean	0.33	0.44	0.51	0.32	0.44	0.51	0.53	0.56	0.76
SD	0.03	0.05	0.04	0.03	0.05	0.04	0.03	0.03	0.04
MIN	0.28	0.28	0.41	0.28	0.31	0.43	0.47	0.52	0.66
MAX	0.39	0.51	0.58	0.37	0.51	0.57	0.56	0.60	0.82

Table 6. Dice similarity coefficient between deformation pairs for the highest (81-100)% ventilation.

Vent.	**ΔV**			**Jacobian**			**HU**		
DIR	OF DM	OF DD	DM DD	OF DM	OF DD	DM DD	OF DM	OF DD	DM DD
Mean	0.33	0.50	0.42	0.32	0.50	0.42	0.41	0.43	0.65
SD	0.03	0.07	0.04	0.03	0.06	0.04	0.03	0.02	0.07
MIN	0.25	0.26	0.36	0.25	0.31	0.36	0.36	0.40	0.52
MAX	0.39	0.58	0.50	0.37	0.58	0.51	0.45	0.46	0.77

Figure 20 (a) and (b) are plots of the DSC for the lowest and highest 20% ventilation for all 20 patients, respectively, for the ΔV, Jacobian, and HU methods calculated using the OF, DM, and DD DIR algorithms. This figure shows the dice comparisons between each DIR method.

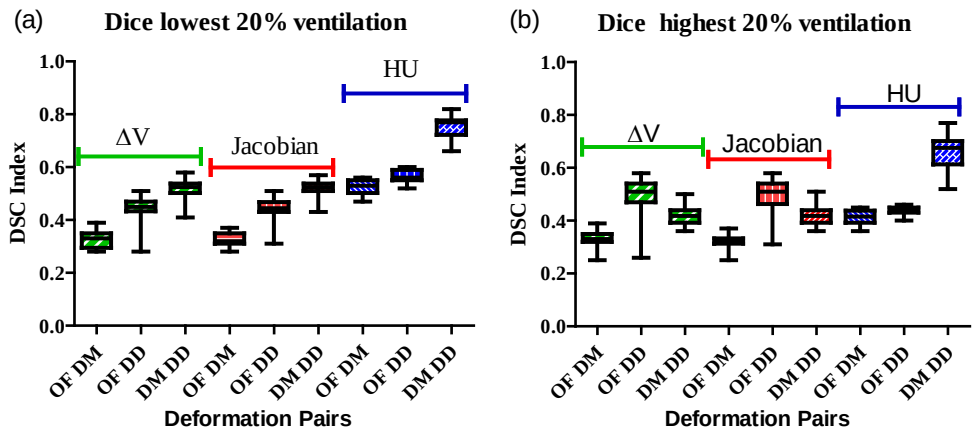

Figure 20. Dice similarity coefficient (DSC) index. (a) Comparisons between OF, DM and DD deformation with ΔV, Jacobian, and HU ventilation for the lowest 20% ventilation, and (b) for the highest 20% ventilation.

Table 7 shows the mean and SD values for ventilation image differences calculated with the ΔV method using OF, DM and DD for DIR. Figure 21 shows a histogram of the differences between ventilations calculated with ΔV and the three DIR methods. Note that the standard deviation between OF-DM and OF-DD is much larger than that of DM-DD indicating a smaller difference between ventilation calculated with DM and DD. The histogram representing DM minus DD is nearer zero compared to the ones for OF minus DM and OF minus DD.

Table 7. Ventilation differences for ΔV comparing deformation methods.

	ΔV		
	OF-DM	OF-DD	DM-DD
Mean	-0.011	-0.012	-0.011
SD	0.27	0.25	0.16

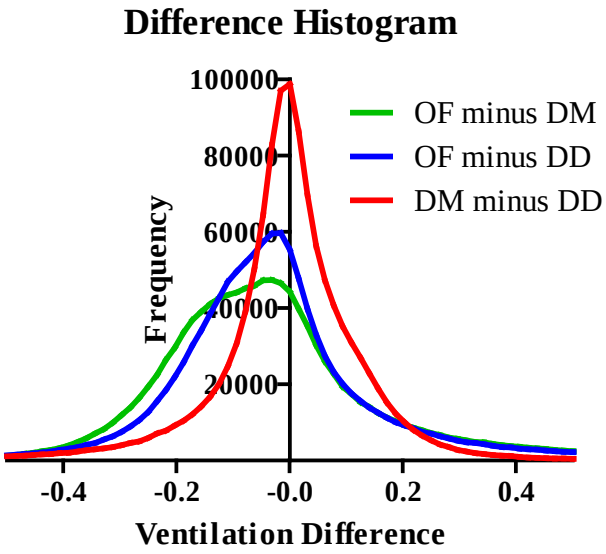

Figure 21. Difference histogram for the ΔV ventilation comparing deformations.

Figure 22 is a graphical display of the ventilation differences between the methods discussed. Note that Figure 22 (c) is generally a darker image, indicating smaller differences between the methods, compared to either of Figure 22 (a) or (b).

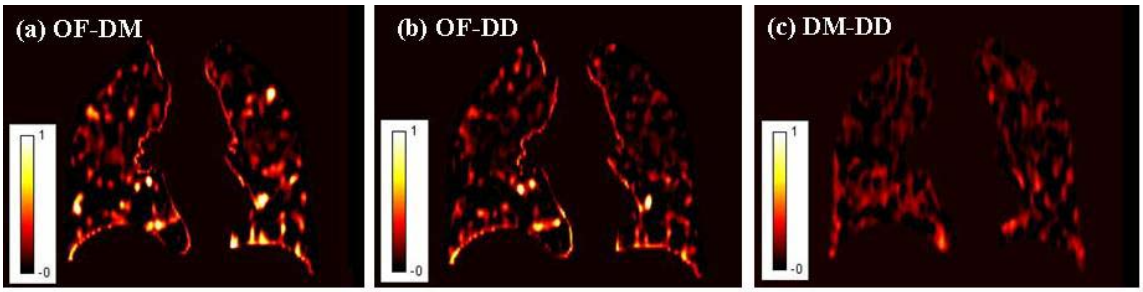

Figure 22. Ventilation image differences for ΔV between (a) OF-DM, (b) OF-DD, and (c) DM-DD.

3.3 Ventilation Dependence on the VA

Figure 23 (a), (b), and (c) show coronal and axial images of the calculated ventilation using the ΔV, Jacobian, and HU ventilation methods with the OF deformable image registration algorithm. By visual observation of Figure 23 we can see that there is a higher degree of overlap between the ΔV and the Jacobian ventilation images.

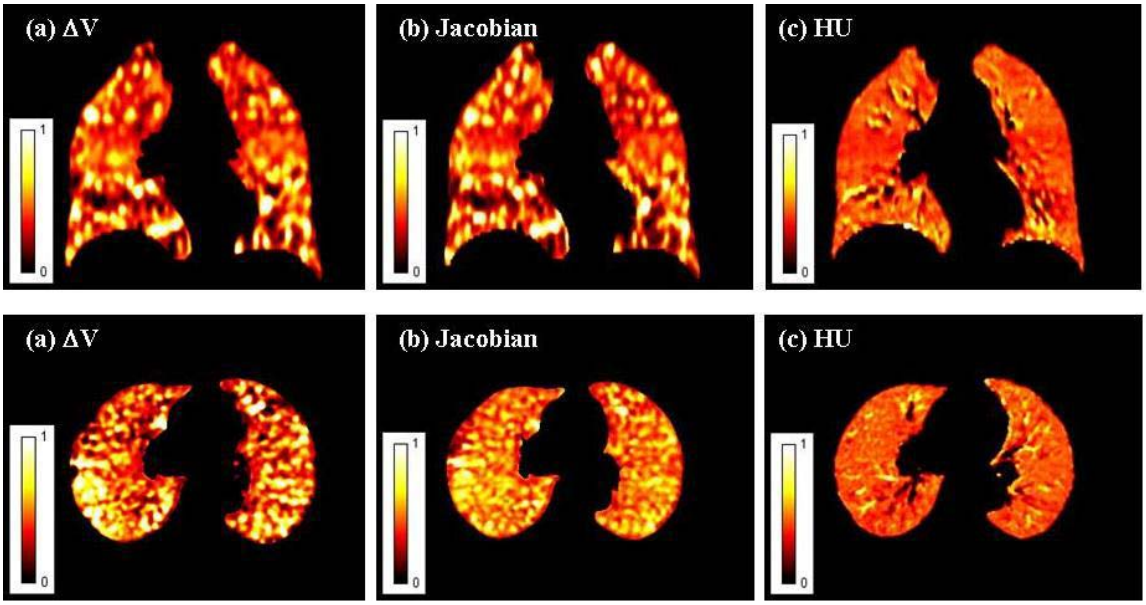

Figure 23. Coronal and axial images of (a) ΔV, (b) Jacobian, and (c) HU ventilation with OF deformation.

Figure 24 (a), (b), and (c) show coronal and axial images of the calculated ventilation using the ΔV, Jacobian, and HU ventilation methods with the DM deformable image registration algorithm.

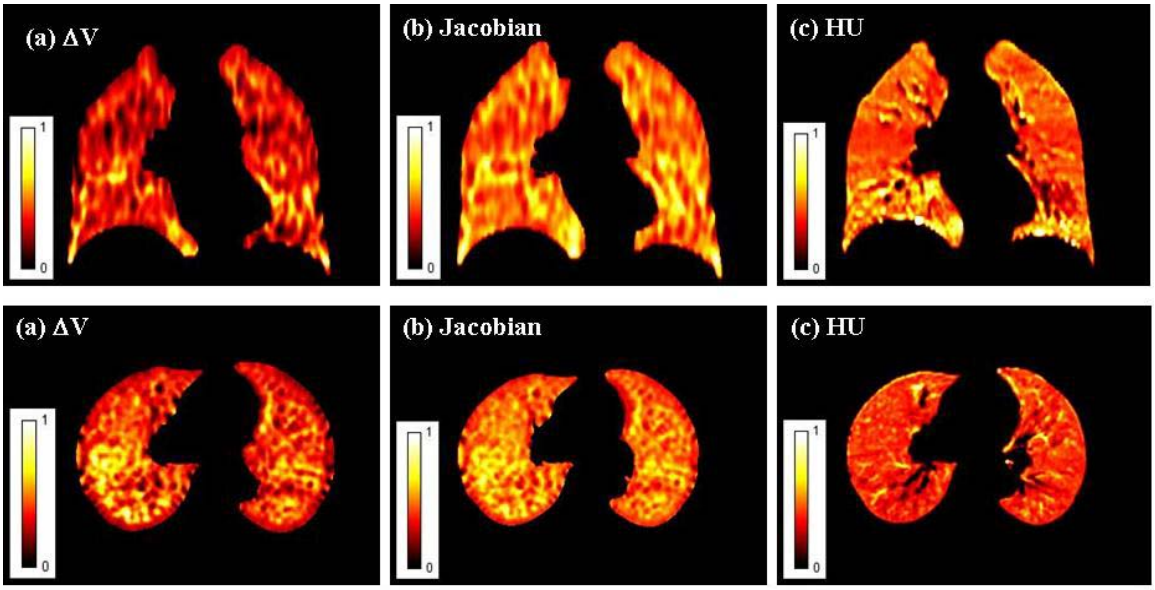

Figure 24. Coronal and axial images of (a) ΔV, (b) Jacobian, and (c) HU ventilation with DM deformation.

Figure 25 (a), (b), and (c) show coronal and axial images of the calculated ventilation using the ΔV, Jacobian, and HU ventilation methods with the DD deformable image registration algorithm.

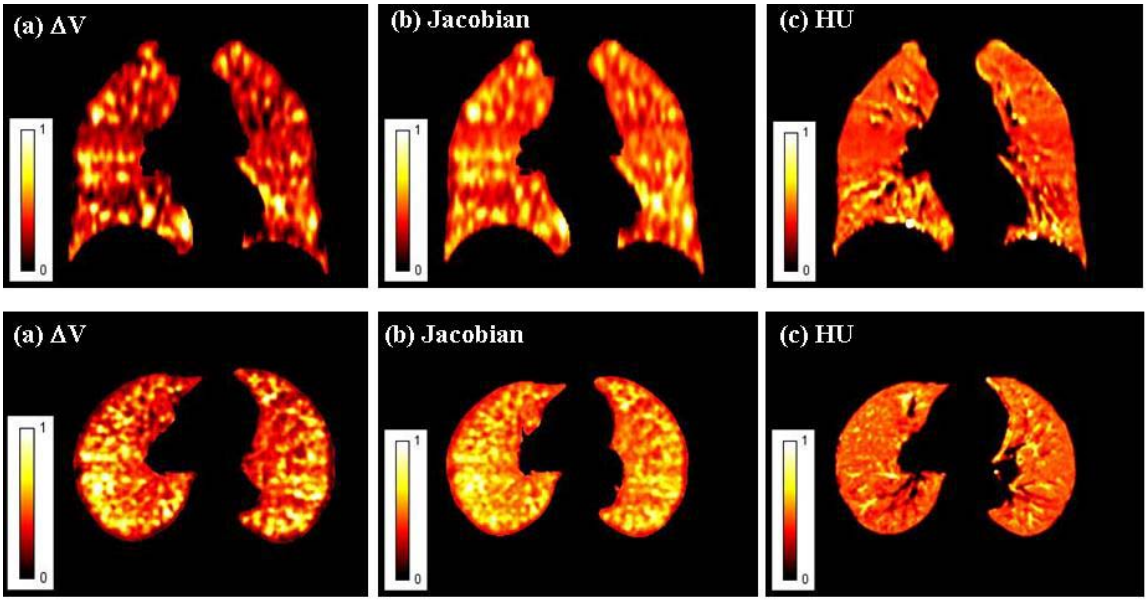

Figure 25. Coronal and axial images of (a) ΔV, (b) Jacobian, and (c) HU ventilation with DD deformation.

The DSC index for using OF as DIR, as shown in Figure 26 and Table 8, was 0.86 ± 0.01 between ΔV and Jacobian, 0.28± 0.04 between ΔV and HU, and 0.28 ± 0.04 between Jacobian and HU respectively. The DSC index for using DM as DIR was 0.88 ± 0.01 between ΔV and Jacobian, 0.34± 0.04 between ΔV and HU, and 0.35 ± 0.04 between Jacobian and HU respectively, and for DD 0.88 ± 0.01, 0.36 ± 0.04 and 0.37 ± 0.04 respectively. The DSC index values for the highest 20% ventilation were close to the ones for the lowest 20% ventilation as shown in Table 9. Detailed DSC values for all twenty patients are given in Tables A1, A2, A3, and A4 in the appendix section.

Table 8. Dice similarity coefficient between ventilation pairs for the lowest (0-20)% ventilation.

DIR	Optical Flow			Diffeomorphic Morphons			Diffeomorphic Demons		
Vent.	ΔV&J	ΔV &HU	J&HU	ΔV &J	ΔV &HU	J&HU	ΔV &J	ΔV &HU	J&HU
Mean	0.86	0.28	0.28	0.88	0.34	0.35	0.88	0.36	0.37
SD	0.01	0.04	0.04	0.01	0.04	0.04	0.01	0.04	0.04
MIN	0.80	0.21	0.21	0.86	0.28	0.28	0.86	0.29	0.29
MAX	0.88	0.35	0.35	0.89	0.41	0.43	0.90	0.41	0.43

Table 9. Dice similarity coefficient between ventilation pairs for the highest (81-100)% ventilation.

DIR	Optical Flow			Diffeomorphic Morphons			Diffeomorphic Demons		
Vent.	ΔV&J	ΔV &HU	J&HU	ΔV &J	ΔV &HU	J&HU	ΔV &J	ΔV &HU	J&HU
Mean	0.83	0.23	0.24	0.84	0.27	0.27	0.86	0.30	0.28
SD	0.01	0.03	0.03	0.01	0.05	0.04	0.02	0.03	0.03
MIN	0.81	0.18	0.18	0.82	0.21	0.21	0.83	0.26	0.23
MAX	0.85	0.31	0.32	0.87	0.41	0.40	0.89	0.36	0.35

Figure 26 (a) and (b) are plots of the DSC index for the lowest and highest 20% ventilation for all 20 patients, respectively, comparing the similarities between the images calculated with ΔV, Jacobian, and HU ventilation algorithms.

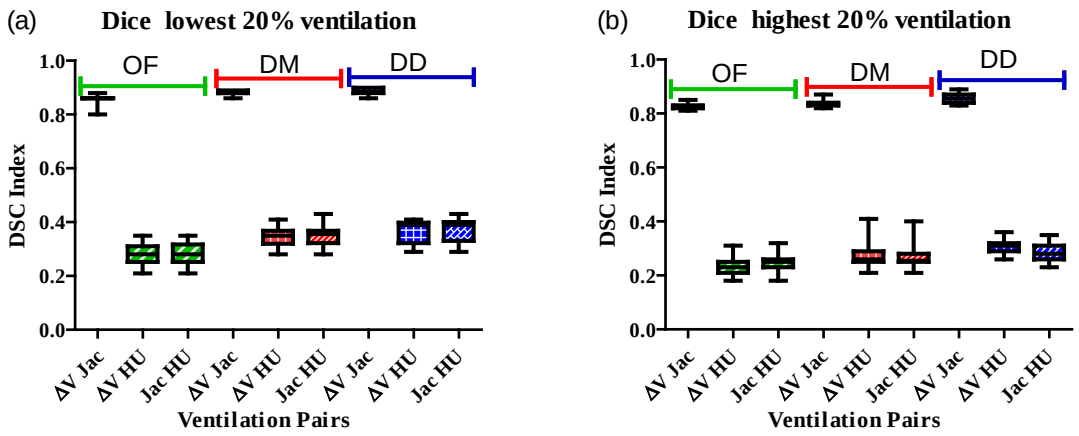

Figure 26. Dice similarity coefficient (DSC) index between ventilation pairs. (a) DSC index for OF, DM, and DD deformation for the lowest 20% ventilation, and (b) DSC index for OF, DM, and DD deformation for the highest 20% ventilation.

Table 10 shows the mean and SD values for ventilation image differences between the ΔV, Jacobian, and HU methods with OF as the DIR method. Figure 27 shows a histogram of the differences between these methods. Note that the differences between the ΔV and HU, and Jacobian and HU are much larger than the differences between the ΔV and Jacobian indicated by the SD in the table and their histograms in the figure. Figure 28 (a) is generally a darker image, indicating smaller differences between the methods, compared to either of Figure 28 (b) or (c).

Table 10. Ventilation differences for OF comparing ventilations.

	OF		
	ΔV-J	ΔV-HU	J-HU
Mean	-0.10	0.015	0.014
SD	0.10	0.29	0.29

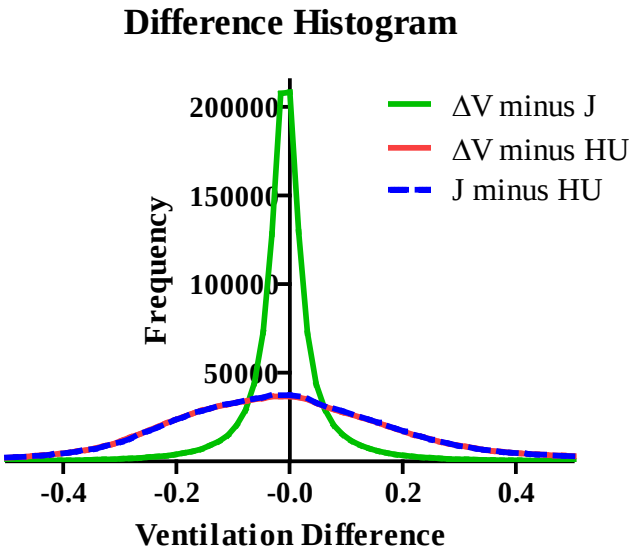

Figure 27. Difference histogram for the ΔV ventilation comparing ventilations.

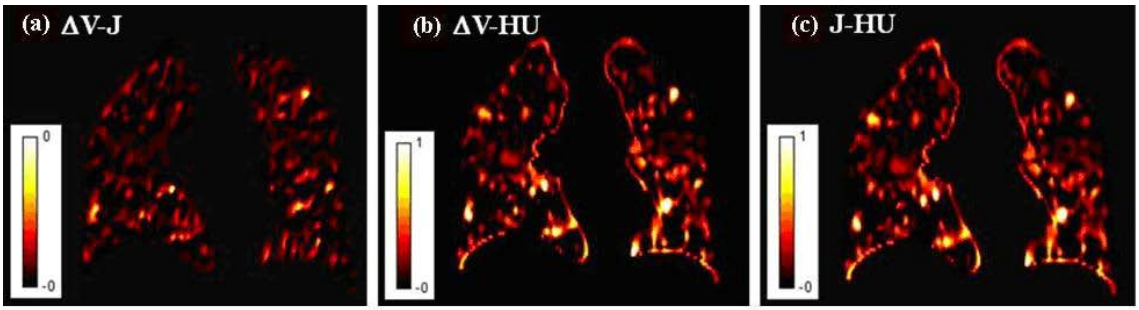

Figure 28. Ventilation image differences for OF between (a) ΔV minus Jacobian, (b) ΔV minus HU, and (c) Jacobian minus HU.

CHAPTER 4 DISCUSSION

Various groups have used different models to validate image registration algorithms. Janssens et al used metallic fiducial markers implanted inside a homogeneous phantom to evaluate deformable image registration with Morphons and Demons. [64] There are several issues with using phantoms for evaluating DIR methods. Phantoms in general are not deformed in the same manner as a normal patient's anatomy; they also deform reproducibly, thus producing superior 4D-CT image sets without the variability of actual patient breathing. The deformations of the phantom may also be more predictable and smoothly varying. Phantoms are a good method for testing DIR, but results may not be directly related to 4D-CT imaging of patients.

In a different study, Janssens et al reported similar results to ours when validating Diffeomorphic Morphons and Diffeomorphic Demons using the POPI model. [74] They found that the mean target registration error for Diffeomorphic Morphons was 0.9±0.5 mm, and a maximum of 2.8 mm, the mean target registration error for Diffeomorphic Morphons was 1.0±0.5 mm and a maximum of 2.8 mm. The reason for the differences between our results may be due to the differences in image resolution as the voxel size for their study was $2\times2\times2$ mm^3.

Wang et al tested the Demons method on three different cases using a model based on real patient data. [75] In the first case they used CT images from a prostate patient, and then mathematically deformed the images in a well defined manner. In the second case they used CT images from a head-and-neck patient, and then mathematically deformed the images, and in the third case they used a deformable pelvis phantom. They found that the mean error for the first case was 0.5±1.5 mm, for the second case 0.2±0.6 mm, and 0.8±0.5 mm for the third case. Although this is a more advanced model than phantom measurements to test the accuracy of the deformation method this method also lacks patient variability and consequently may overestimate the accuracy of the technique.

Castillo et al evaluated the OF method using a large number of landmarks [76]. They tested image registration with voxel size 5×5×5 mm^3 and found that the mean registration error for this method was 6.9±0.1 mm. This method is similar to the model we used for our validation because it is based on anatomical landmarks. The voxel size used for this study is quite large and may not reflect the clinical situation; the CT voxel size of the POPI model used in our validation was 0.97×0.97×2 mm^3. Additionally, they tested a landmark based deformable image registration method and found that it performed better than the OF method (error of 2.05±0.02 mm). As one would expect, using landmarks to evaluate a landmark based algorithm may yield too optimistic results. Additionally, Castillo et al found the error in OF was greater than using no DIR at all for 4 out of the 5 cases they reported.

Voxel size also has an influence on the accuracy of the DIR. In all these validation studies the voxel size will directly determine a lower limit of accuracy that can be reached using DIR. For example the slice thickness is the limiting factor on the accuracy of the landmark points in the superior–inferior direction because a point may lie in between two slices which would make it hard to identify by the radiologist on the two image sets. In addition the image sets used are from a 4D-CT, which may make the identification of landmarks less clear than identifying landmarks on a breath-hold CT. Therefore, we consider the registration accuracy in validation study for the three DIR algorithms to be acceptable as the mean target registration errors are below the slice thickness. This is comparable to the validation study for Demon's algorithm reported by Vandemeulebroucke et al.

The POPI model is published and used by many groups for validation studies. [66, 67, 74, 77] The task of manually selecting landmarks is difficult, tedious, and time consuming. In addition, selecting landmarks in the end-expiration phase is more difficult because of the change of density of the lung. [67] Given the difficulties of manual landmark selection, only one set of 4D-CT data is available in the model. Thus in this study, one set of data with 39 points was used in the validation.

DIR algorithms are also evaluated by studying the image difference between the deformed image and the target image. The smaller the difference between the deformed and the target images the better the DIR algorithm. HU values in the lung for the CT sets used ranged from -922 to near 0. This large range in values can potentially lead to large

differences when comparing two images if they are not perfectly aligned. In the case of the differences between the deformed image and the target image, large differences in HU are due to the variations at interfaces within the lung. The interfaces between the blood vessels and other parts of the lung may lead to large differences in HU between image sets.

While the validation results show that all three DIR methods perform well, we speculate that how DIR methods address the imperfection of the 4D-CT images may contribute to some of the inaccuracies observed.[78] Each method has its own strengths and weaknesses. The DM method is based on matching edges and lines in a voxel and if an image has an artifact then that artifact would propagate throughout the process of image deformation. On the other hand, the OF and DD methods are intensity based registration methods, and they may deal differently with an image artifact. Additionally, the DM and DD methods have smoothing filters applied to their deformation fields which may lead to additional differences in image deformation.

When compared to the HU method, ΔV and Jacobian are very different. DSC index shows only about 30% similarity between these methods and the HU method [see Figure 26]. The HU method is a density based ventilation calculation method. DSC index, shown in Figure 20, suggests that the HU method is less dependent on the DIR used and depends more on the CT image quality due to the inherent noise of HUs in normal CT imaging.

The dependence on the DIR used appears to be smaller for the HU ventilation algorithm. If most of the lung is similar in density, i.e. a mixture of blood vessels and alveolar, then the effects of any misregistrations will be small because of the similar densities. However, if there is a misregistration between lung and much denser tissue, such as chest wall or large artery, then the change in HU is quite significant. The HU algorithm screens for these voxels with very large change in HUs and then excludes these voxels in the ventilation image. However HUs for low density objects tend to be quite noisy. To overcome this issue Castillo et al [29] smoothed the DIR using a cube of 5×5×5 voxels then also smoothed the ventilation image using a box filter of 9×9×3 voxels.

The dependence of the ventilation image on the DIR seems to be more significant for the ΔV and Jacobian methods. With these algorithms a large misregistrations will result in a significant over or under estimation of the local ventilation. While smoothing does mitigate this effect somewhat, the benefit of smoothing has a smaller effect for these algorithms than for the HU algorithm. However, the benefits of high resolution ventilation imaging degrade with smoothing.

The need for smoothing for the ΔV and Jacobian methods comes from these misregistrations of the end expiration and inspiration image sets. The source of the misregistration issues comes directly from the 4D-CT itself. Currently there are two commercially available techniques for 4D-CT imaging. The first uses a cine acquisition (GE medical systems), which bins rapidly axial images based on a breathing trace. This method produces slab artifacts that are clearly visualized on sagital and coronal

reconstructions with the width of each slab corresponding to the transaxial collimation used in the 4D-CT acquisition. The second acquisition technique bins the sinogram data itself then reconstructs each phase on this binned sinogram data (Philips and Siemens). The artifacts are generally less pronounced in this imaging technique; however, both methods produce significant artifacts when patients breathe irregularly. Due to limitations of CT scanners and the ability of a patient to breathe reproducibly most 4D image sets present with imaging artifacts that are unique to 4D acquisitions.

CHAPTER 5 CONCLUSION

We validated all three DIR methods (intensity based and structure based methods) using the POPI model, which is a landmark based model. We also used image differences to evaluate the accuracy of DIR methods. For normal end-expiration to end-inspiration registration all three methods show a maximum target registration error of less than 4 mm, or two voxels, with insignificant differences between them (P=0.37). The mean target registration error for each of the registration algorithms was less than the slice thickness of the 3D CT volumes, which suggests that the deformable registrations done be either of the methods are quite accurate. Additionally, image differences between the target and the deformed images did not show much variation between the DIR methods.

Ventilation calculation from 4D-CT demonstrates some degree of dependency on the DIR algorithm employed. HU shows a smaller dependence on the choice of DIR, however, its weakness lies with its dependence on the image quality due to the effects of noise in the CT image intensities. Similarities between ΔV and Jacobian are higher than between ΔV and HU and between Jacobian and HU. This shows that ΔV and Jacobian are very similar, but HU is a very different ventilation calculation method.

CHAPTER 6 FUTURE WORK

There are two projects that have been planned to continue the study on high resolution ventilation imaging based on 4D-CT. The first is to compare calculated ventilation images based on 4D-CT to the ones acquired with SPECT. We hypothesize that high resolution ventilation image based on 4D-CT correlates with the current state-of-the-art ventilation image using SPECT. We plan to test this hypothesis by comparing regions of poor ventilation on SPECT images to ventilation images based on 4D-CT using the DSC index.

The second project is to do a before and after study on patients to determine the effects of radiation on ventilation. Lung toxicity is one of the biggest concerns in thoracic radiation treatment planning. It would be ideal to assess lung ventilation in order to derive structures that could be avoided during treatment and therefore to minimize dose to the part of the lung that functions better.

CHAPTER 7 REFERENCES

1. American Cancer Society., "Cancer facts & figures," (American Cancer Society, Atlanta, GA, 2010), pp. v.
2. M. V. Graham, J. A. Purdy, B. Emami, W. Harms, W. Bosch, M. A. Lockett and C. A. Perez, "Clinical dose-volume histogram analysis for pneumonitis after 3D treatment for non-small cell lung cancer (NSCLC)," Int J Radiat Oncol Biol Phys **45**, 323-329 (1999).
3. H. K. Lee, A. A. Vaporciyan, J. D. Cox, S. L. Tucker, J. B. Putnam, Jr., J. A. Ajani, Z. Liao, S. G. Swisher, J. A. Roth, W. R. Smythe, G. L. Walsh, R. Mohan, H. H. Liu, D. Mooring and R. Komaki, "Postoperative pulmonary complications after preoperative chemoradiation for esophageal carcinoma: correlation with pulmonary dose-volume histogram parameters," Int J Radiat Oncol Biol Phys **57**, 1317-1322 (2003).
4. L. B. Marks, M. T. Munley, D. P. Spencer, G. W. Sherouse, G. C. Bentel, J. Hoppenworth, M. Chew, R. J. Jaszczak, R. E. Coleman and L. R. Prosnitz, "Quantification of radiation-induced regional lung injury with perfusion imaging," Int J Radiat Oncol Biol Phys **38**, 399-409 (1997).

5. B. Emami, J. Lyman, A. Brown, L. Coia, M. Goitein, J. E. Munzenrider, B. Shank, L. J. Solin and M. Wesson, "Tolerance of normal tissue to therapeutic irradiation," Int J Radiat Oncol Biol Phys **21**, 109-122 (1991).

6. E. S. Evans, C. A. Hahn, Z. Kocak, S.-M. Zhou and L. B. Marks, "The Role of Functional Imaging in the Diagnosis and Management of Late Normal Tissue Injury," Seminars in Radiation Oncology **17**, 72-80 (2007).

7. L. B. Marks, "Physiology-based studies of radiation-induced normal tissue injury," Radiother Oncol **51**, 101-103 (1999).

8. L. B. Marks, S. M. Bentzen, J. O. Deasy, F. M. Kong, J. D. Bradley, I. S. Vogelius, I. El Naqa, J. L. Hubbs, J. V. Lebesque, R. D. Timmerman, M. K. Martel and A. Jackson, "Radiation Dose-Volume Effects in the Lung," International Journal of Radiation Oncology Biology Physics **76**, S70-S76 (2010).

9. L. B. Marks, M. T. Munley, G. C. Bentel, S. M. Zhou, D. Hollis, C. Scarfone, G. S. Sibley, F. M. Kong, R. Jirtle, R. Jaszczak, R. E. Coleman, V. Tapson and M. Anscher, "Physical and biological predictors of changes in whole-lung function following thoracic irradiation," Int J Radiat Oncol Biol Phys **39**, 563-570 (1997).

10. L. B. Marks, G. W. Sherouse, M. T. Munley, G. C. Bentel and D. P. Spencer, "Incorporation of functional status into dose-volume analysis," Med Phys **26**, 196-199 (1999).

11. G. J. Kutcher and C. Burman, "Calculation of complication probability factors for non-uniform normal tissue irradiation: the effective volume method," Int J Radiat Oncol Biol Phys **16**, 1623-1630 (1989).

12. J. T. Lyman and A. B. Wolbarst, "Optimization of radiation therapy, III: A method of assessing complication probabilities from dose-volume histograms," Int J Radiat Oncol Biol Phys **13**, 103-109 (1987).

13. C. Burman, G. J. Kutcher, B. Emami and M. Goitein, "Fitting of normal tissue tolerance data to an analytic function," Int J Radiat Oncol Biol Phys **21**, 123-135 (1991).

14. L. Cozzi, F. M. Buffa and A. Fogliata, "Comparative analysis of dose volume histogram reduction algorithms for normal tissue complication probability calculations," Acta Oncol **39**, 165-171 (2000).

15. C. S. Hamilton, L. Y. Chan, D. L. McElwain and J. W. Denham, "A practical evaluation of five dose-volume histogram reduction algorithms," Radiother Oncol **24**, 251-260 (1992).

16. W. A. Altemeier, S. McKinney and R. W. Glenny, "Fractal nature of regional ventilation distribution," J Appl Physiol **88**, 1551-1557 (2000).

17. R. W. Glenny, S. Bernard, H. T. Robertson and M. P. Hlastala, "Gravity is an important but secondary determinant of regional pulmonary blood flow in upright primates," J Appl Physiol **86**, 623-632 (1999).

18. J. Petersson, A. Sanchez-Crespo, S. A. Larsson and M. Mure, "Physiological imaging of the lung: single-photon-emission computed tomography (SPECT)," J Appl Physiol **102**, 468-476 (2007).

19. R. Jeraj, Y. Cao, R. K. Ten Haken, C. Hahn and L. Marks, "Imaging for assessment of radiation-induced normal tissue effects," Int J Radiat Oncol Biol Phys **76**, S140-144 (2010).

20. A. Gottschalk, H. D. Sostman, R. E. Coleman, J. E. Juni, J. Thrall, K. A. McKusick, J. W. Froelich and A. Alavi, "Ventilation-perfusion scintigraphy in the PIOPED study. Part II. Evaluation of the scintigraphic criteria and interpretations," J Nucl Med **34**, 1119-1126 (1993).

21. S. Fanti, M. Farsad, L. Mansi, H. Gutte, J. Mortensen and A. KjÃ¦r, "Ventilation/Perfusion Imaging with SPECT-CT Atlas of SPECT-CT," (Springer Berlin Heidelberg), pp. 195-202.

22. B. Harris, D. Bailey, S. Miles, E. Bailey, K. Rogers, P. Roach, P. Thomas, M. Hensley and G. G. King, "Objective analysis of tomographic ventilation-perfusion scintigraphy in pulmonary embolism," Am J Respir Crit Care Med **175**, 1173-1180 (2007).

23. J. Petersson, A. Sanchez-Crespo, M. Rohdin, S. Montmerle, S. Nyren, H. Jacobsson, S. A. Larsson, S. G. Lindahl, D. Linnarsson, R. W. Glenny and M. Mure, "Physiological evaluation of a new quantitative SPECT method measuring regional ventilation and perfusion," J Appl Physiol **96**, 1127-1136 (2004).

24. K. Suga, "Technical and analytical advances in pulmonary ventilation SPECT with xenon-133 gas and Tc-99m-Technegas," Annals of Nuclear Medicine **16**, 303-310 (2002).

25. G. Musch, J. D. Layfield, R. S. Harris, M. F. Melo, T. Winkler, R. J. Callahan, A. J. Fischman and J. G. Venegas, "Topographical distribution of pulmonary perfusion and ventilation, assessed by PET in supine and prone humans," J Appl Physiol **93**, 1841-1851 (2002).

26. M. F. Vidal Melo, D. Layfield, R. S. Harris, K. O'Neill, G. Musch, T. Richter, T. Winkler, A. J. Fischman and J. G. Venegas, "Quantification of regional ventilation-perfusion ratios with PET," J Nucl Med **44**, 1982-1991 (2003).

27. N. Ogasawara, K. Suga, Y. Kawakami, T. Yamashita, M. Zaki and N. Matsunaga, "Assessment of regional lung function impairment in airway obstruction and pulmonary embolic dogs with combined noncontrast electrocardiogram-gated perfusion and gadolinium diethylenetriaminepentaacetic acid aerosol magnetic resonance images," J Magn Reson Imaging **20**, 46-55 (2004).

28. Y. Ohno and H. Hatabu, "Basics concepts and clinical applications of oxygen-enhanced MR imaging," European journal of radiology **64**, 320-328 (2007).

29. R. Castillo, E. Castillo, J. Martinez and T. Guerrero, "Ventilation from four-dimensional computed tomography: density versus Jacobian methods," Physics in Medicine and Biology **55**, 4661-4685 (2010).

30. K. Ding, J. E. Bayouth, J. M. Buatti, G. E. Christensen and J. M. Reinhardt, "4DCT-based measurement of changes in pulmonary function following a course of radiation therapy," Med Phys **37**, 1261-1272 (2010).

31. T. Guerrero, K. Sanders, E. Castillo, Y. Zhang, L. Bidaut, T. S. Pan and R. Komaki, "Dynamic ventilation imaging from four-dimensional computed tomography," Physics in Medicine and Biology **51**, 777-791 (2006).

32. T. Guerrero, K. Sanders, J. Noyola-Martinez, E. Castillo, Y. Zhang, R. Tapia, R. Guerra, Y. Borghero and R. Komaki, "Quantification of regional ventilation from treatment planning CT," Int J Radiat Oncol Biol Phys **62**, 630-634 (2005).

33. J. M. Reinhardt, G. E. Christensen, E. A. Hoffman, K. Ding and K. Cao, "Registration-derived estimates of local lung expansion as surrogates for regional ventilation," Inf Process Med Imaging **20**, 763-774 (2007).

34. J. M. Reinhardt, K. Ding, K. Cao, G. E. Christensen, E. A. Hoffman and S. V. Bodas, "Registration-based estimates of local lung tissue expansion compared to xenon CT measures of specific ventilation," Med Image Anal **12**, 752-763 (2008).

35. B. A. Simon, "Non-invasive imaging of regional lung function using x-ray computed tomography," J Clin Monit Comput **16**, 433-442 (2000).

36. T. Yamamoto, S. Kabus, J. von Berg, C. Lorenz, E. S. Mittra, A. Quon, B. W. Loo and P. J. Keall, "Four-dimensional computed tomography-based pulmonary ventilation imaging for adaptive functional guidance in radiotherapy," Journal of Thoracic Oncology **4**, S959-S960 (2009).

37. G. Zhang, T. J. Dilling, C. W. Stevens and K. M. Forster, "Functional lung imaging in thoracic cancer radiotherapy," Cancer Control **15**, 112-119 (2008).

38. G. Zhang, T. C. Huang, T. J. Dilling, C. W. Stevens and K. M. Forster, "Derivation of High-Resolution Pulmonary Ventilation Using Local Volume Change in Four-Dimensional CT Data," IFMBE Proceedings **25**, 4 (2009).

39. C. J. Cabahug, M. McPeck, L. B. Palmer, A. Cuccia, H. L. Atkins and G. C. Smaldone, "Utility of technetium-99m-DTPA in determining regional ventilation," J Nucl Med **37**, 239-244 (1996).

40. S. M. McGuire, S. Zhou, L. B. Marks, M. Dewhirst, F.-F. Yin and S. K. Das, "A methodology for using SPECT to reduce intensity-modulated radiation therapy

(IMRT) dose to functioning lung," International Journal of Radiation Oncology*Biology*Physics **66**, 1543-1552 (2006).

41. J. Palmer, U. Bitzen, B. Jonson and M. Bajc, "Comprehensive ventilation/perfusion SPECT," J Nucl Med **42**, 1288-1294 (2001).

42. K. Suga, "Technical and analytical advances in pulmonary ventilation SPECT with xenon-133 gas and Tc-99m-Technegas," Ann Nucl Med **16**, 303-310 (2002).

43. D. P. Schuster, C. Anderson, J. Kozlowski and N. Lange, "Regional pulmonary perfusion in patients with acute pulmonary edema," J Nucl Med **43**, 863-870 (2002).

44. J. T. Bushberg, J. A. Seibert, E. M. Leidholdt Jr. and J. M. Boone, *The Essential Physics of Medical Imaging*, 2nd ed. (Lippincott Williams & Wilkins, Philadelphia, 2002).

45. B. Misselwitz, A. Muhler, I. Heinzelmann, J. C. Bock and H. J. Weinmann, "Magnetic resonance imaging of pulmonary ventilation. Initial experiences with a gadolinium-DTPA-based aerosol," Invest Radiol **32**, 797-801 (1997).

46. A. B. Montgomery, H. Paajanen, R. C. Brasch and J. F. Murray, "Aerosolized gadolinium-DTPA enhances the magnetic resonance signal of extravascular lung water," Invest Radiol **22**, 377-381 (1987).

47. K. Suga, Y. Yuan, N. Ogasawara, T. Tsukuda and N. Matsunaga, "Altered clearance of gadolinium diethylenetriaminepentaacetic acid aerosol from bleomycin-injured dog lungs: initial observations," Am J Respir Crit Care Med **167**, 1704-1710 (2003).

48. R. Loffler, C. J. Muller, M. Peller, H. Penzkofer, M. Deimling, M. Schwaiblmair, J. Scheidler and M. Reiser, "Optimization and evaluation of the signal intensity change in multisection oxygen-enhanced MR lung imaging," Magn Reson Med **43**, 860-866 (2000).

49. T. Stavngaard, L. V. SÃ¸gaard, J. Mortensen, L. G. Hanson, J. r. Schmiedeskamp, A. K. Berthelsen and A. Dirksen, "Hyperpolarised ³He MRI and ^{81m}Kr SPECT in chronic obstructive pulmonary disease," in *European Journal of Nuclear Medicine and Molecular Imaging*, *Vol. 32*, (Springer Berlin / Heidelberg, 2005), pp. 448-457.

50. P. J. Keall, G. S. Mageras, J. M. Balter, R. S. Emery, K. M. Forster, S. B. Jiang, J. M. Kapatoes, D. A. Low, M. J. Murphy, B. R. Murray, C. R. Ramsey, M. B. Van Herk, S. S. Vedam, J. W. Wong and E. Yorke, "The management of respiratory motion in radiation oncology report of AAPM Task Group 76," Med Phys **33**, 3874-3900 (2006).

51. R. Bajcsy and S. Kovacic, "Multiresolution elastic matching," Computer Vision, Graphics, and Image Processing **46**, 1-21 (1989).

52. J. V. Hajnal, D. L. G. Hill and D. J. Hawkes, "Medical Image Registration," in *CRC Press*, (2001).

53. T. Guerrero, G. Zhang, T. C. Huang and K. P. Lin, "Intrathoracic tumour motion estimation from CT imaging using the 3D optical flow method," Physics in Medicine and Biology **49**, 4147-4161 (2004).

54. G. Zhang, T. C. Huang, T. Guerrero, K. P. Lin, C. Stevens, G. Starkschall and K. Forster, "Use of three-dimensional (3D) optical flow method in mapping 3D

anatomic structure and tumor contours across four-dimensional computed tomography data," Journal of Applied Clinical Medical Physics **9**, 59-69 (2008).

55. G. G. Zhang, T. C. Huang, K. M. Forster, K. P. Lin, C. Stevens, E. Harris and T. Guerrero, "Dose mapping: validation in 4D dosimetry with measurements and application in radiotherapy follow-up evaluation," Comput Methods Programs Biomed **90**, 25-37 (2008).

56. T. Yamamoto and et al., "Investigation of four-dimensional computed tomography-based pulmonary ventilation imaging in patients with emphysematous lung regions," Physics in Medicine and Biology **56**, 2279.

57. T. Yamamoto, S. Kabus, J. von Berg, C. Lorenz and P. J. Keall, "Impact of Four-dimensional CT-derived Pulmonary Ventilation Images on Radiotherapy Treatment Planning for Lung Cancer," International Journal of Radiation Oncology Biology Physics **75**, S443-S443 (2009).

58. S. S. Beauchemin and J. L. Barron, "The computation of optical flow," ACM Comput. Surv. **27**, 433-466 (1995).

59. B. K. P. Horn and B. G. Schunck, "Determining optical flow," Artificial Intelligence **17**, 185-203 (1981).

60. C. Taylor, A. Colchester, X. Pennec, P. Cachier and N. Ayache, "Understanding the Demon's Algorithm: 3D Non-rigid Registration by Gradient Descent," in *Medical Image Computing and Computer-Assisted Intervention – MICCAI'99*, *Vol. 1679,* (Springer Berlin / Heidelberg, 1999), pp. 597-605.

61. J. P. Thirion, "Image matching as a diffusion process: an analogy with Maxwell's demons," Med Image Anal **2**, 243-260 (1998).

62. T. Vercauteren, X. Pennec, A. Perchant and N. Ayache, "Diffeomorphic demons: Efficient non-parametric image registration," Neuroimage **45**, S61-S72 (2009).

63. A. Wrangsjo, J. Pettersson and H. Knutsson, "Non-rigid registration using morphons," Image Analysis, Proceedings **3540**, 501-510 (2005).

64. G. Janssens, J. O. de Xivry, S. Fekkes, A. Dekker, B. Macq, P. Lambin and W. van Elmpt, "Evaluation of nonrigid registration models for interfraction dose accumulation in radiotherapy," Med Phys **36**, 4268-4276 (2009).

65. C. Vaman, D. Staub, J. Williamson and M. J. Murphy, "A method to map errors in the deformable registration of 4DCT images," Medical Physics **37**, 5765-5776 (2010).

66. J. Vandemeulebroucke, D. Sarrut and P. Clarysse, "The POPI-model, a point-validated pixel-based breathing thorax model.," XVth International Conference on the Use of Computers in Radiation Therapy (ICCR) (2007).

67. D. Sarrut, V. Boldea, S. Miguet and C. Ginestet, "Simulation of four-dimensional CT images from deformable registration between inhale and exhale breath-hold CT scans," Medical Physics **33**, 605-617 (2006).

68. H. Kalviainen, J. Parkkinen, A. Kaarna, A. Wrangsjö, J. Pettersson and H. Knutsson, "Non-rigid Registration Using Morphons," in *Image Analysis, Vol. 3540,* (Springer Berlin / Heidelberg, 2005), pp. 501-510.

69. X. J. Gu, H. Pan, Y. Liang, R. Castillo, D. S. Yang, D. J. Choi, E. Castillo, A. Majumdar, T. Guerrero and S. B. Jiang, "Implementation and evaluation of various demons deformable image registration algorithms on a GPU," Physics in Medicine and Biology **55**, 207-219 (2010).

70. G. G. Zhang, T. C. Huang, T. Dilling, C. Stevens and K. M. Forster, presented at the World Congress on Medical Physics and Biomedical Engineering, Munich, Germany, 2009 (unpublished).

71. P. J. Keall, G. Starkschall, H. Shukla, K. M. Forster, V. Ortiz, C. W. Stevens, S. S. Vedam, R. George, T. Guerrero and R. Mohan, "Acquiring 4D thoracic CT scans using a multislice helical method," Physics in Medicine and Biology **49**, 2053-2067 (2004).

72. L. R. Dice, "Measures of the Amount of Ecologic Association Between Species," Ecology **26**, 297-302 (1945).

73. A. C. Riegel, J. Y. Chang, S. S. Vedam, V. Johnson, P.-C. M. Chi and T. Pan, "Cine Computed Tomography Without Respiratory Surrogate in Planning Stereotactic Radiotherapy for Non-Small-Cell Lung Cancer," International Journal of Radiation Oncology*Biology*Physics **73**, 433-441 (2009).

74. G. Janssens, L. Jacques, J. Orban de Xivry, X. Geets and B. Macq, "Diffeomorphic registration of images with variable contrast enhancement," Int J Biomed Imaging **2011**, 891585 (2011).

75. H. Wang, L. Dong, J. O'Daniel, R. Mohan, A. S. Garden, K. K. Ang, D. A. Kuban, M. Bonnen, J. Y. Chang and R. Cheung, "Validation of an accelerated 'demons' algorithm for deformable image registration in radiation therapy," Physics in Medicine and Biology **50**, 2887-2905 (2005).

76. R. Castillo, E. Castillo, R. Guerra, V. E. Johnson, T. McPhail, A. K. Garg and T. Guerrero, "A framework for evaluation of deformable image registration spatial

accuracy using large landmark point sets," Physics in Medicine and Biology **54**, 1849-1870 (2009).

77. S. Kabus, T. Klinder, K. Murphy, B. Ginneken, C. Lorenz and J. P. Pluim, "Evaluation of 4D-CT Lung Registration," in *Proceedings of the 12th International Conference on Medical Image Computing and Computer-Assisted Intervention: Part I,* (Springer-Verlag, London, UK, 2009).

78. T. Yamamoto, U. Langner, B. W. Loo, Jr., J. Shen and P. J. Keall, "Retrospective analysis of artifacts in four-dimensional CT images of 50 abdominal and thoracic radiotherapy patients," Int J Radiat Oncol Biol Phys **72**, 1250-1258 (2008).

APPENDIX A EXTRA TABLES

Table A1. Raw values of Dice similarity coefficient (DSC) index between deformations for the lowest (0-20)% ventilation for all 20 patients.

	ΔV			J			HU		
Case number	**OF DM**	**OF DD**	**DM DD**	**OF DM**	**OF DD**	**DM DD**	**OF DM**	**OF DD**	**DM DD**
1	0.33	0.45	0.52	0.31	0.45	0.52	0.53	0.59	0.77
2	0.28	0.39	0.50	0.28	0.35	0.51	0.47	0.52	0.76
3	0.33	0.44	0.54	0.32	0.43	0.54	0.51	0.55	0.77
4	0.37	0.47	0.55	0.37	0.46	0.56	0.53	0.57	0.81
5	0.32	0.47	0.53	0.33	0.47	0.53	0.53	0.56	0.76
6	0.31	0.41	0.53	0.31	0.41	0.53	0.53	0.57	0.76
7	0.32	0.44	0.55	0.31	0.44	0.55	0.55	0.58	0.80
8	0.39	0.46	0.58	0.37	0.45	0.57	0.55	0.60	0.80
9	0.33	0.48	0.51	0.33	0.47	0.51	0.55	0.60	0.78
10	0.28	0.28	0.51	0.28	0.31	0.52	0.52	0.52	0.76
11	0.29	0.41	0.41	0.31	0.43	0.43	0.50	0.55	0.71
12	0.29	0.45	0.51	0.29	0.44	0.51	0.53	0.56	0.77
13	0.33	0.46	0.48	0.33	0.46	0.48	0.50	0.53	0.71
14	0.35	0.46	0.53	0.35	0.44	0.53	0.51	0.54	0.82
15	0.29	0.44	0.43	0.29	0.44	0.44	0.55	0.59	0.69
16	0.39	0.50	0.53	0.37	0.50	0.53	0.56	0.60	0.77
17	0.31	0.44	0.44	0.32	0.45	0.44	0.55	0.55	0.71
18	0.35	0.51	0.51	0.35	0.51	0.51	0.50	0.56	0.66
19	0.33	0.43	0.53	0.32	0.43	0.53	0.50	0.55	0.77
20	0.36	0.51	0.54	0.36	0.50	0.54	0.55	0.59	0.77

Table A2. Raw values of Dice similarity coefficient (DSC) index between deformations for the highest (81-100)% ventilation for all 20 patients.

	ΔV			J			HU		
Case number	**OF DM**	**OF DD**	**DM DD**	**OF DM**	**OF DD**	**DM DD**	**OF DM**	**OF DD**	**DM DD**
1	0.33	0.58	0.43	0.32	0.58	0.43	0.43	0.45	0.70
2	0.29	0.40	0.40	0.29	0.40	0.40	0.40	0.40	0.68
3	0.33	0.50	0.43	0.32	0.51	0.43	0.39	0.40	0.67
4	0.39	0.54	0.48	0.37	0.52	0.48	0.44	0.43	0.73
5	0.33	0.55	0.41	0.32	0.54	0.41	0.40	0.45	0.62
6	0.36	0.48	0.44	0.36	0.48	0.44	0.40	0.43	0.63
7	0.35	0.52	0.45	0.33	0.53	0.45	0.39	0.43	0.68
8	0.35	0.54	0.43	0.35	0.54	0.44	0.37	0.40	0.68
9	0.31	0.51	0.39	0.29	0.51	0.40	0.40	0.45	0.69
10	0.25	0.26	0.40	0.25	0.31	0.39	0.45	0.40	0.73
11	0.32	0.45	0.44	0.31	0.45	0.43	0.45	0.45	0.62
12	0.33	0.51	0.41	0.32	0.50	0.41	0.44	0.44	0.71
13	0.32	0.46	0.36	0.32	0.45	0.36	0.43	0.44	0.60
14	0.36	0.50	0.50	0.33	0.47	0.51	0.43	0.44	0.77
15	0.31	0.53	0.36	0.32	0.53	0.36	0.36	0.46	0.53
16	0.32	0.54	0.37	0.32	0.55	0.37	0.39	0.45	0.61
17	0.32	0.47	0.37	0.31	0.48	0.37	0.44	0.46	0.52
18	0.35	0.56	0.40	0.36	0.55	0.40	0.43	0.43	0.57
19	0.33	0.47	0.44	0.33	0.46	0.44	0.43	0.46	0.67
20	0.35	0.57	0.43	0.33	0.56	0.43	0.40	0.44	0.70

Table A3. Raw values of Dice similarity coefficient (DSC) index between ventilation algorithms for the lowest (0-20)% ventilation for all 20 patients.

	OF			DM			DD		
Case number	**ΔV & J**	**ΔV & HU**	**J & HU**	**ΔV & J**	**ΔV & HU**	**J & HU**	**ΔV & J**	**ΔV & HU**	**J &HU**
1	0.86	0.31	0.32	0.87	0.36	0.36	0.88	0.41	0.43
2	0.80	0.25	0.21	0.86	0.28	0.31	0.88	0.35	0.36
3	0.85	0.28	0.28	0.89	0.35	0.36	0.87	0.36	0.36
4	0.88	0.35	0.35	0.88	0.35	0.35	0.86	0.40	0.40
5	0.86	0.25	0.26	0.88	0.33	0.33	0.89	0.37	0.39
6	0.86	0.26	0.26	0.89	0.39	0.39	0.89	0.39	0.39
7	0.86	0.28	0.28	0.88	0.41	0.43	0.88	0.40	0.41
8	0.86	0.29	0.31	0.89	0.39	0.39	0.88	0.40	0.40
9	0.87	0.31	0.31	0.88	0.33	0.33	0.88	0.39	0.39
10	0.86	0.21	0.21	0.88	0.28	0.28	0.87	0.29	0.29
11	0.86	0.21	0.23	0.89	0.29	0.29	0.90	0.29	0.31
12	0.86	0.26	0.25	0.87	0.35	0.36	0.90	0.31	0.31
13	0.86	0.28	0.28	0.89	0.32	0.32	0.89	0.33	0.33
14	0.86	0.31	0.31	0.88	0.32	0.32	0.86	0.39	0.37
15	0.86	0.23	0.23	0.89	0.35	0.36	0.90	0.29	0.31
16	0.85	0.32	0.32	0.88	0.40	0.41	0.90	0.39	0.40
17	0.84	0.26	0.26	0.88	0.32	0.33	0.90	0.32	0.33
18	0.86	0.31	0.32	0.88	0.35	0.35	0.90	0.39	0.39
19	0.86	0.28	0.28	0.88	0.35	0.36	0.88	0.41	0.41
20	0.87	0.32	0.32	0.89	0.37	0.37	0.89	0.39	0.39

Table A4. Raw values of Dice similarity coefficient (DSC) index between ventilation algorithms for the highest (81-100)% ventilation for all 20 patients.

	OF			DM			DD		
Case number	**ΔV & J**	**ΔV & HU**	**J & HU**	**ΔV & J**	**ΔV & HU**	**J & HU**	**ΔV & J**	**ΔV & HU**	**J &HU**
1	0.81	0.21	0.25	0.83	0.21	0.21	0.83	0.31	0.28
2	0.82	0.21	0.21	0.84	0.23	0.23	0.85	0.31	0.31
3	0.83	0.23	0.25	0.83	0.21	0.21	0.85	0.29	0.26
4	0.83	0.21	0.25	0.84	0.26	0.25	0.83	0.26	0.23
5	0.83	0.26	0.28	0.84	0.26	0.26	0.86	0.33	0.32
6	0.83	0.25	0.26	0.84	0.29	0.28	0.87	0.33	0.31
7	0.83	0.23	0.23	0.84	0.25	0.25	0.84	0.31	0.28
8	0.82	0.18	0.20	0.83	0.25	0.23	0.84	0.28	0.26
9	0.82	0.23	0.25	0.83	0.25	0.25	0.84	0.29	0.29
10	0.83	0.18	0.18	0.84	0.25	0.26	0.84	0.29	0.31
11	0.85	0.21	0.23	0.87	0.28	0.25	0.89	0.29	0.28
12	0.83	0.26	0.28	0.83	0.29	0.28	0.87	0.32	0.28
13	0.82	0.21	0.23	0.84	0.28	0.26	0.86	0.28	0.25
14	0.82	0.23	0.25	0.85	0.25	0.25	0.83	0.31	0.28
15	0.84	0.20	0.21	0.85	0.32	0.31	0.89	0.26	0.25
16	0.82	0.23	0.26	0.82	0.32	0.31	0.86	0.32	0.29
17	0.83	0.31	0.32	0.83	0.29	0.28	0.88	0.36	0.35
18	0.83	0.25	0.28	0.86	0.41	0.40	0.87	0.31	0.28
19	0.83	0.25	0.26	0.84	0.32	0.32	0.86	0.33	0.32
20	0.82	0.20	0.23	0.84	0.26	0.25	0.85	0.29	0.26